J. Fluid Mech. (2009), *vol.* 625, *pp.* 167–203.
doi:10.1017/S0022112008005442 Printed in the United Kingdom

The fluid trampoline: droplets bouncing on a soap film

TRISTAN GILET[1] AND JOHN W. M. BUSH[2]†

[1]Group for Research and Applications in Statistical Physics, Department of Physics, University of Liege, 4000 Liege, Belgium

[2]Department of Mathematics, Massachusetts Institute of Technology, Cambridge, MA 02139, USA

(Received 8 March 2008 and in revised form 4 December 2008)

We present the results of a combined experimental and theoretical investigation of droplets falling onto a horizontal soap film. Both static and vertically vibrated soap films are considered. In the static case, a variety of behaviours were observed, including bouncing, crossing and partial coalescence. A quasi-static description of the soap film shape yields a force–displacement relation that provides excellent agreement with experiment, and allows us to model the film as a nonlinear spring. This approach yields an accurate criterion for the transition between droplet bouncing and crossing. Moreover, it allows us to rationalize the observed constancy of the contact time and scaling for the coefficient of restitution in the bouncing states. On the vibrating film, a variety of bouncing behaviours were observed, including simple and complex periodic states, multi-periodicity and chaos. A simple theoretical model is developed that captures the essential physics of the bouncing process, reproducing all observed bouncing states. The model enables us to rationalize the observed coexistence of multiple periodic bouncing states by considering the dependence of the energy transferred to the droplet on the phase of impact. Quantitative agreement between model and experiment is deduced for simple periodic modes, and qualitative agreement for more complex periodic and chaotic bouncing states. Analytical solutions are deduced in the limit of weak forcing and dissipation, yielding insight into the contact time and periodicity of the bouncing states.

1. Introduction

A remarkable series of experiments has recently been conducted by Couder and co-workers. First, they demonstrated that a droplet is able to bounce indefinitely without coalescing on the surface of a vertically vibrated liquid bath (Couder *et al.* 2005*a*). In certain regimes, a bouncing droplet moves laterally through its interaction with its own wave field (Couder *et al.* 2005*b*; Protière *et al.* 2005; Protière, Boudaoud & Couder 2006). As the droplet thus walks across the surface, its wave field probes the surroundings, detecting solid obstacles that may be used to guide the droplets. When many such walkers are present, they may interact to form stable orbits or lattice structures (Lieber *et al.* 2007). More surprising yet, when a droplet passes

† Email address for correspondence: bush@math.mit.edu

through a slit formed by two submerged objects, it is deflected in such a way that the distribution of deviation angles is analogous to Young's fringes observed for photons and electrons: the droplet and its wave are thus diffracted (Couder & Fort 2006). The bouncing droplet experiment is thus exceptionally rich, exhibiting features of optics (diffraction), quantum systems (wave–particle duality), statistical physics (phase transitions) and astronomy (complex orbital motions). We here explore a simple variation on their system that exhibits all the features of low-dimensional chaos.

When a droplet is placed on a quiescent fluid bath, it ultimately collapses into the bath due to gravity; however, this merger is generally delayed because the air layer between the droplet and the bath must first drain to a thickness at which Van der Waals forces between droplet and bath become important, approximately 100 nm (Charles & Mason 1960*a*). The resulting coalescence may take a number of distinct forms. Complete coalescence arises when the entirety of the drop merges with the underlying reservoir. Partial coalescence arises when only some fraction of the drop coalesces, leaving behind a smaller daughter droplet that is ejected from the bath and bounces several times before itself undergoing a partial coalescence (Mahajan 1930; Charles & Mason 1960*b*; Thoroddsen & Takehara 2000; Honey & Kavehpour 2006). This coalescence cascade continues until the daughter droplet becomes sufficiently small that viscosity comes into play, and complete coalescence occurs. Blanchette & Bigioni (2006) demonstrated that partial coalescence is possible only when $Oh = \mu/\sqrt{\rho\sigma R} < 0.026$, where μ is the dynamic viscosity of the droplet, ρ its density, σ its surface tension and R its radius. The influence of viscosity on partial coalescence has been further examined by Chen, Mandre & Feng (2006) and Gilet *et al.* (2007*a*). A variety of novel partial coalescence events will be reported in § 2 in our experimental study of droplets impinging on a soap film.

The coalescence of droplets into an underlying fluid reservoir may be delayed by a variety of methods (Neitzel & Dell'Aversana 2002). For example, Dell'Aversana, Banavar & Koplik (1996) demonstrated that drop coalescence may be delayed by a temperature gradient between drop and reservoir, since the resulting Marangoni stresses may serve to resist the drainage of the intervening air layer. Couder *et al.* (2005*a*) demonstrate that drop coalescence may be entirely eliminated by vertical oscillations of the underlying bath; here, the intervening air layer is replenished by the flow generated as the drop lifts from the surface. The lifetime of a bouncing droplet on a vibrating reservoir may range from minutes to days (Terwagne, Vandewalle & Dorbolo 2007).

Stable droplet bouncing requires that the vertical acceleration Γ of the bath be higher than a threshold Γ_C. For high-viscosity droplets (typically 500 cS), Couder *et al.* (2005*a*) have shown that Γ_C increases smoothly with increasing forcing frequency f. Gilet *et al.* (2008) and Dorbolo *et al.* (2008) have demonstrated that relatively low viscosity droplets (0.65–100 cS) may also bounce on a highly viscous bath. In this case, Γ_C decreases with increasing f, until reaching the resonant frequency of the droplet; thereafter, it increases smoothly until diverging for a critical frequency ($f_c \geqslant 100$ Hz). The larger the droplet, the higher the threshold Γ_c. For $\Gamma < \Gamma_c$, large droplets partially coalesce until they reach a size appropriate for stable bouncing (Gilet, Vandewalle & Dorbolo 2007*b*).

Bouncing has been examined in a variety of geometries. Considerable effort has been directed towards characterizing the bouncing of solid objects. For example,

the bouncing of an inelastic ball on a solid substrate is a canonical model for the onset of chaos (Mehta & Luck 1993). The bouncing of solid beads on an elastic membrane was examined by Courbin *et al.* (2006), who showed that the time of contact between the bead and membrane tends to a constant in the high-speed limit. Bouncing droplets have been studied in various configurations. Legendre, Daniel & Guiraud (2005) examined the impact of a droplet suspended in a surrounding fluid. Criteria for bouncing versus coalescence for droplets striking the free surface of a fluid bath have been considered by several investigators (e.g. Jayaratne & Mason 1964), most recently by Pan & Law (2007). Richard, Clanet & Quéré (2002) examined droplets bouncing on hydrophobic surfaces, and reported a constant contact time for high-speed impacts. The constancy of the impact time for a droplet on a soap film will be reported in § 2.2 and exploited in our subsequent theoretical developments.

A trampoline imparts a vertical force owing to deflection of the elastic membrane under a tension T. A characteristic bouncing frequency for an object of mass m on such a membrane may be defined as $\sqrt{T/m}$ (Graff 1975). For an elastic ball of radius R, the characteristic bouncing frequency is given by $\sqrt{ER/m}$, where E is the ball's Young's modulus (Graff 1975). The system considered here, specifically a droplet on a soap film, has common features with both problems. In particular, the natural frequencies of both the film and droplet scale as $\sqrt{\sigma/m}$, where m is the mass of the droplet and σ is the surface tension. Periodic bouncing is achieved on a trampoline by forcing the system at its natural frequency; likewise, we shall observe that drops bounce on a soap film only when the forcing frequency is comparable to the natural frequency of the film.

The impact of a droplet on a stationary soap film was first described by Courbin & Stone (2006). For a droplet with radius R and incident speed U striking a soap film with surface tension σ, the Weber number, $We = \rho U^2 R/\sigma$, prescribes the relative magnitudes of the initial kinetic energy of the droplet and the interfacial energy of the system. At low We, the drop was observed to bounce off the soap film, while for high We, it passed through without breaking the film. In the latter circumstance, the leading edge of the drop first coalesces with the film, so the drop is imbedded in the film as it crosses; as it exits the film, its trailing edge emerges without breaking the film, which is said to 'self-heal'. LeGoff *et al.* (2008) examined a solid particle falling through a series of films, and characterized the energy lost with each impact. In § 2.2, we shall report a variety of partial coalescence events that arise in this same system; moreover, we measure the critical We for the transition between bouncing and crossing, a value that we rationalize in § 3.2.

The experimental configuration examined in our study is detailed in § 2. In our first experiment, we examine a falling droplet striking a stationary horizontal soap film. In the second, we examine the effects of vertical oscillations of the soap film on the impacting droplet. Experimental observations are reported in § 2, where particular attention is given to cataloguing the variety of partial coalescence events observed, to refining the bouncing-to-crossing criterion of LeGoff *et al.* (2008) and to characterizing the bouncing states observed on the vibrating film. In § 3, the film-induced force on the droplet is characterized, revealing that the soap film may be simply modelled as a nonlinear spring. In § 4, we exploit this inference in developing a theoretical model for the drop trajectory that allows us to rationalize our observations of periodic and chaotic bouncing on a soap film. The principal conclusions of our study are reviewed in § 5.

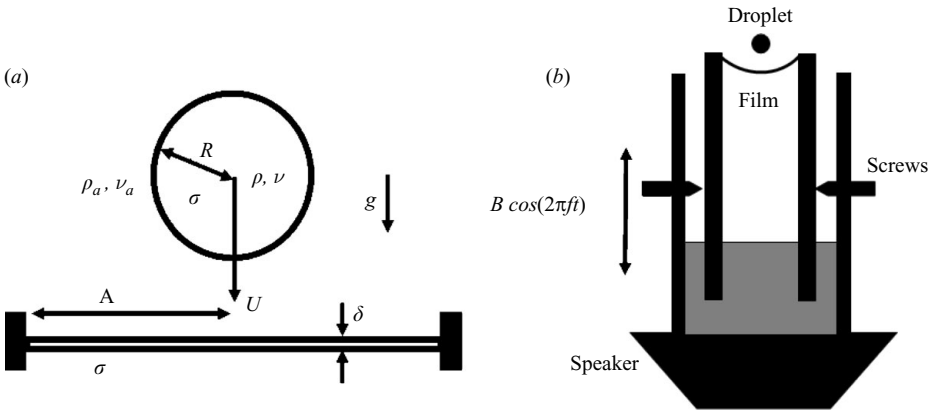

FIGURE 1. Experimental set-up. (*a*) Without vibration: a droplet strikes a horizontal soap film fixed on a ring. (*b*) With vibration: the soap film is pinned at the end of the inner tube, which is vertically vibrated by a speaker. The arrangement with the outer cylinder ensures a downward curvature of the film, and so stabilizes the bouncing droplet on axis.

2. Experiments

2.1. *Experimental method*

In the first series of experiments (figure 1*a*), a horizontal soap film is held fixed on a thin ring of internal radius $A = 0.8$ cm as it is struck by a falling droplet. A droplet of constant radius $R = 0.08$ cm is released above the soap film from an insulin syringe. The impact speed U is varied between 10 and 100 cm s^{-1} by changing the release height. Experiments are recorded from the side with a high-speed video camera (Redlake MASD PCI Motionscope) with acquisition rate 1000 fps and resolution 256×256 pixel. For our typical field of view, the characteristic pixel size is 50 μm. Measurements of drop position and film shape are made via image processing.

In the second series of experiments (figure 1*b*), the soap film is vertically vibrated so that periodic droplet bouncing may arise. A horizontal soap film is created at the end of a plexiglas tube of radius $A = 1.6$ cm fixed on a subwoofer speaker (Sony SA-W3800) that vibrates vertically in a sinusoidal fashion. The motion of the speaker is recorded on an accelerometer: the frequency and amplitude of the oscillation are measured from the output signal. The amplitude B of the vibration generates a maximum acceleration between 0.15 and 3 g; the frequency f ranges between 20 and 80 Hz. A groove is made at the end of the tube in order to pin the soap film at a fixed height. To avoid the practical difficulties of levelling the soap film, the tube is put in a larger concentric tube (figure 1*b*) that is partially filled with water and fixed to the speaker. The soap film is created on the inner tube while the tube is immersed in the fluid reservoir, so that an air column is trapped between the soap film and the liquid bath. The inner tube is then moved slightly upwards before fixing it to the outer cylinder with screws. The resulting low pressure in the air column deflects the soap film downwards at its centre; the resulting film curvature stabilizes the bouncing droplet on axis.

The liquid used for both the droplet and the soap film was a mixture of water, glycerol and commercial soap (Dove®). The concentration of soap is $\sim 1\,\%$ by volume. The viscosity of the liquid is altered by varying the concentration of glycerol.

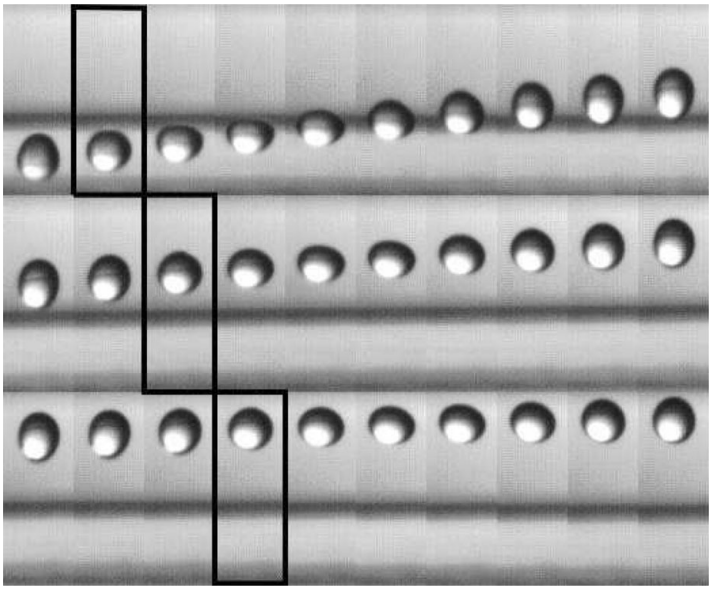

FIGURE 2. Natural oscillations of a droplet in free fall. The time between successive images is 1 ms. Framed images correspond to the transition from a prolate to an oblate shape, and indicate a vibration period of 11 ms.

Most of the experiments were performed with a mixture of 80 % water and 20 % glycerol, which corresponds to a viscosity $\nu = 2\,\mathrm{cS}$ and density $\rho = 1.05\,\mathrm{g\,cm^{-3}}$.

Surface tension measurements accurate to 0.5 % were taken with a Kruss K10 Tensiometer via the Wilhelmy plate method. A mean value of $\sigma = 23.6 \pm 0.6\,\mathrm{dyn\,cm^{-1}}$ was found with values observed between 20 and $25\,\mathrm{dyn\,cm^{-1}}$. The surface tension was also estimated from the natural oscillations of a droplet in free fall. Rayleigh (see for example Landau & Lifchitz 1959) demonstrated that σ may be deduced from the period T of an oscillating droplet according to

$$\sigma = \frac{3\pi m}{8T^2}, \tag{2.1}$$

where $m = 2.25 \times 10^{-3}$ g is the mass of the droplet. As seen in figure 2, $T \simeq 11$ ms, which gives $\sigma \simeq 22\ \mathrm{dyn\,cm^{-1}}$, a value consistent with that measured directly.

The droplet impact experiment is characterized by 10 physical variables: the droplet radius R, the film radius A and thickness δ, the density and the kinematic viscosity of the liquid (ρ, ν) and air (ρ_a, ν_a), the surface tension σ, the gravitational acceleration g and the vertical impact speed U. Two additional parameters are needed to describe the vertically vibrated system, namely the frequency f and amplitude B of the sinusoidal excitation. The range of experimental parameters considered in our study is reported in table 1. For this system, nine independent dimensionless numbers can be formed (table 2). For a given fluid and geometry (drop and frame size), six of these dimensionless groups are fixed, while three are variables: We, Γ and ω.

2.2. *Stationary film*

In our study of impacting droplets, $\beta = \frac{A}{R} = 10$ and $Oh = 0.015$ were held fixed ($\nu = 2\,\mathrm{cS}$) and We was varied from 1 to 30 by varying the release height. As previously

Variable	Name	Range
R	Droplet radius	0.08 cm
A	Soap film radius	0.8–1.6 cm
δ	Soap film thickness	$\sim$1 μm
U	Impact speed	17.5–166 cm s^{-1}
ρ	Liquid density	1.05 g cm^{-3}
ν	Liquid kinematic viscosity	0.89–17 cS
ρ_a	Air density	0.00122 g cm^{-3}
ν_a	Air kinematic viscosity	15 cS
σ	Surface tension	22 dyn cm^{-1}
g	Gravity acceleration	981 cm s^{-2}
B	Forcing amplitude	6×10^{-4} – 0.2 cm
f	Forcing frequency	20–80 Hz

TABLE 1. Physical variables arising in our study.

Variable	Name	Definition	Signification	Range
m	Drop mass	$4\pi\rho R^3/3$		2.25×10^{-3} g
τ_c	Capillary time	$\sqrt{m/\sigma}$		0.01 s
We	Weber	$\rho R U^2/\sigma$	Inertia/surface tension	1–30
Bo	Bond	$mg/\sigma R$	Gravity/surface tension	1.25
Oh	Ohnesorge	$\nu\sqrt{\rho}/\sqrt{\sigma R}$	Viscosity/surface tension	0.007–0.13
	Viscosity ratio	ν_a/ν		0.88–7.5
	Density ratio	ρ_a/ρ		0.0011
β	Aspect ratio	R/A		10 or 20
	Aspect ratio	δ/A		10^{-4}
Ω	Angular frequency	$2\pi f \tau_c$		1.27–5
Γ	Acceleration	$4\pi^2 B f^2/g$	Forcing acceleration/gravity	0.15–3

TABLE 2. Key dimensional quantities and dimensionless groups arising in our study.

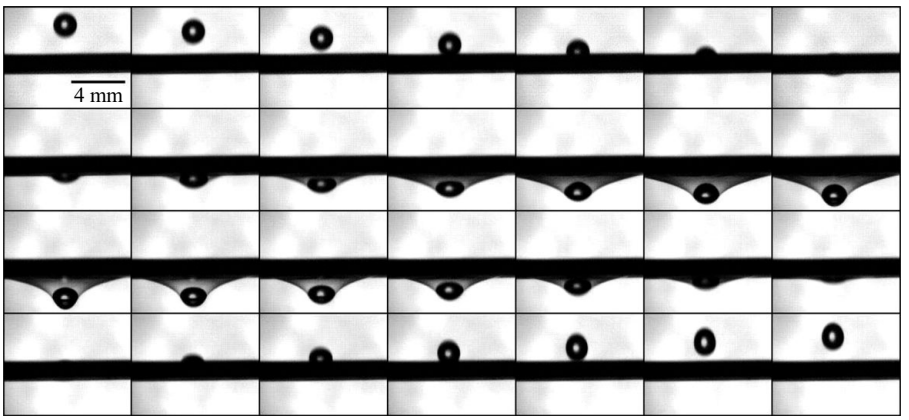

FIGURE 3. Droplet bouncing on a soap film at $We = 8.8$. Frames are taken every millisecond.

observed by Courbin & Stone (2006), the droplet bounces on the soap film for low We (figure 3). At high We, the drop crosses the soap film without breaking it (figure 4).

During a bouncing event (figure 3), the kinetic energy of the falling droplet is primarily converted into surface energy of the distorted soap film during impact;

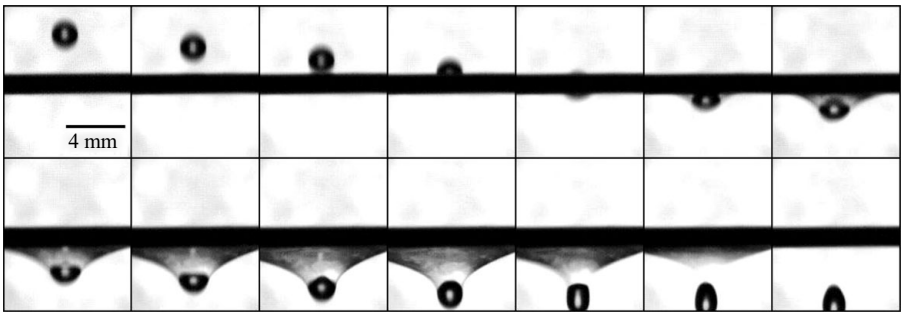

FIGURE 4. Droplet passing through a soap film at $We = 25$. Frames are taken every millisecond.

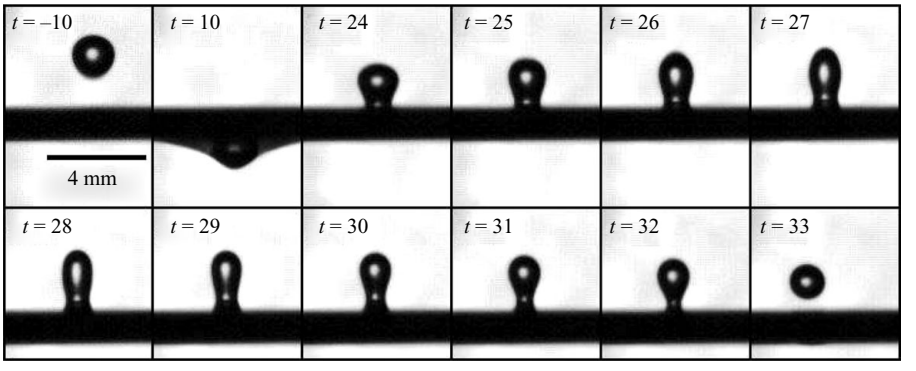

FIGURE 5. Partial coalescence of a droplet on a soap film at $We = 2.5$. Time is indicated in milliseconds. The daughter droplet is smaller than the incident droplet owing to the fluid captured by the soap film.

thereafter, the bulk of this energy is restored to the droplet's kinetic energy. To avoid coalescence, the droplet must never touch the soap film: a thin intervening air layer must persist. As this layer thins, the resulting lubrication pressure deforms the underlying film. At impact, the droplet becomes oblate, but recovers a roughly spherical shape when the soap film deflection is maximal. As the drop is ejected, it again becomes oblate. For the sequence illustrated in figure 3, the contact time t_c, during which the droplet is in the immediate vicinity of the soap film, is 18 ms. In a crossing event (figure 4), the soap film is not able to absorb the initial kinetic energy of the droplet: as the droplet passes through, the film reforms. The analogous self-healing of liquid sheets has been described by Taylor & Howarth (1959) and Taylor & Michael (1973).

In addition to pure bouncing and crossing events, a variety of intermediate partial coalescence events were observed, in which some fraction of the impinging droplet remains trapped as a lens within the soap film. The result of this partial merger is a smaller daughter droplet and possibly accompanying satellite droplets. Unlike partial coalescence on a fluid bath (Charles & Mason 1960*b*; Blanchette & Bigioni 2006; Gilet *et al.* 2007*a*), the ratio between the radii of the daughter and parent droplets is often larger than 0.5. The variety of observed partial coalescence events are illustrated in figures 5–9. The parent droplet can emerge either above (figure 5)

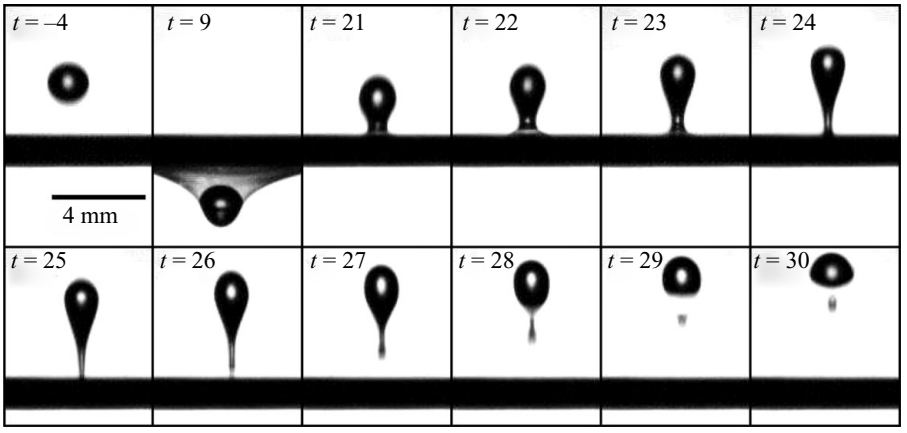

FIGURE 6. Partial coalescence of a droplet on a soap film at $We = 10$. Time is indicated in milliseconds. Note the single satellite droplet formed at the tail of the daughter droplet.

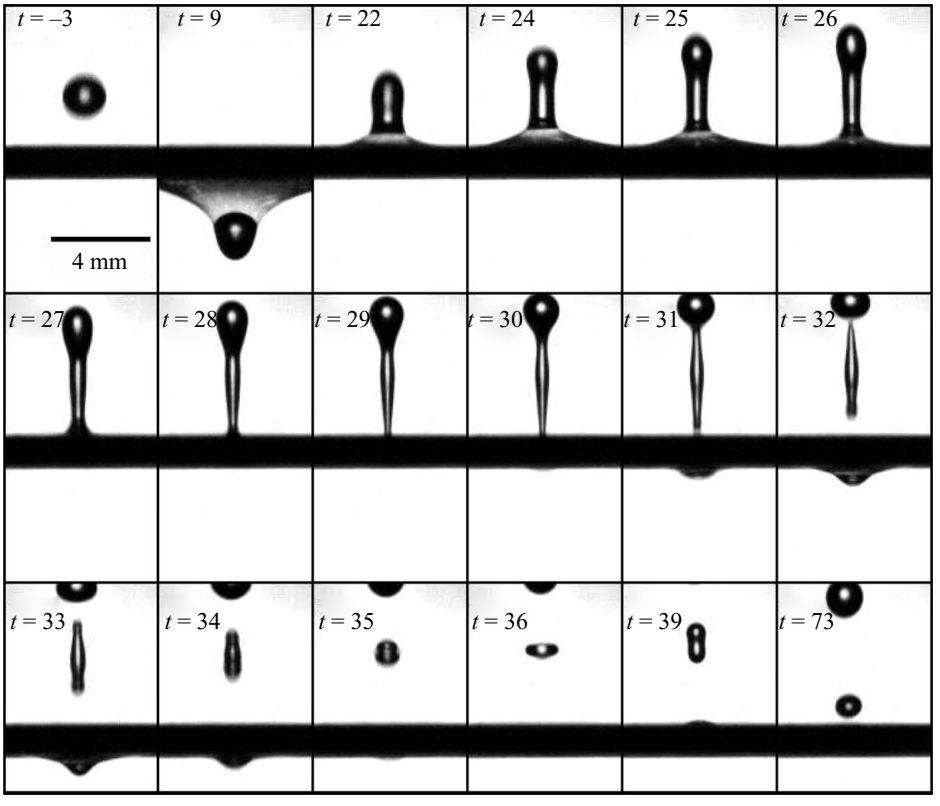

FIGURE 7. Partial coalescence of a droplet on a soap film at $We = 14$. Time is indicated in milliseconds. Note that the satellite droplet is nearly as large as the daughter droplet.

or below (figure 8) the soap film. Figure 9 illustrates a sequence in which a daughter drop is ejected upwards while the parent drop continues downwards. In figure 10, the likelihood of bouncing and crossing is represented as a function of We. While partial coalescence was observed for $2 < We < 16$, the transition between

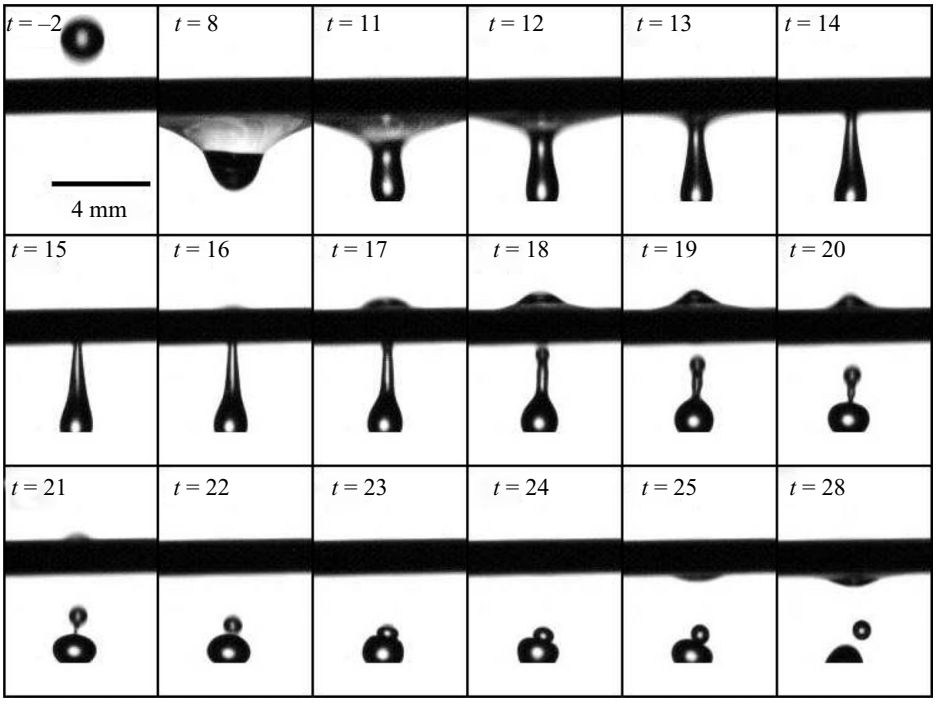

FIGURE 8. Partial coalescence of a droplet on a soap film at $We = 15$. Time is indicated in milliseconds. A satellite droplet is formed.

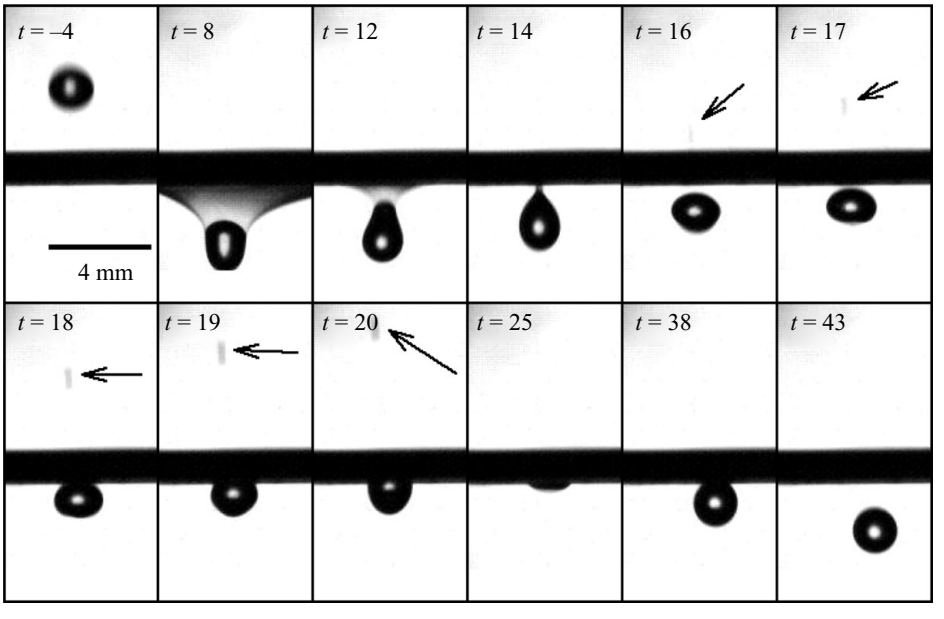

FIGURE 9. Partial coalescence of a droplet on a soap film at $We = 16$. Time is indicated in milliseconds. While the daughter droplet passes through the film, a small satellite droplet (indicated with an arrow) is ejected upwards.

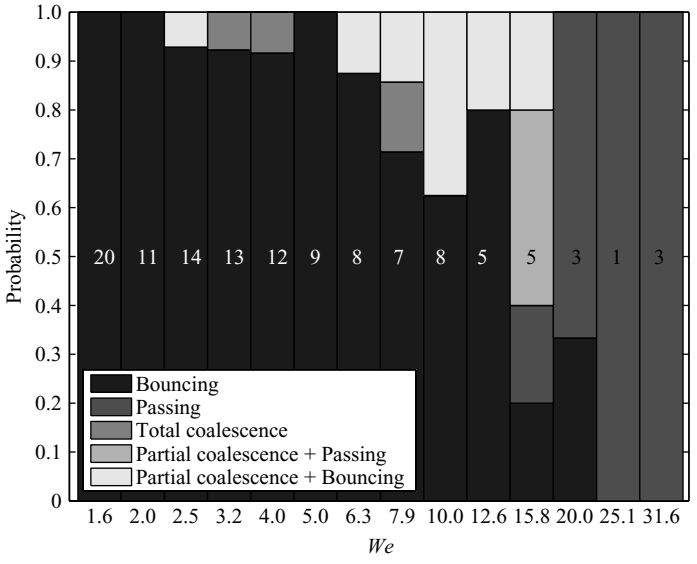

FIGURE 10. Transition from bouncing to crossing for impact on a stationary film. The probability of different events is represented as a function of We. The number of events in each class is reported in the middle of the columns. The transition between bouncing and passing occurs for a critical Weber number $We^* \simeq 16$. Partial coalescence events take place over the interval $2 < We^* < 16$.

bouncing and crossing regimes occurs at $We^* \simeq 16$, an observation to be rationalized in § 3.2.

We proceed by characterizing two important bouncing parameters: the contact time and the energy dissipated during a single bounce. The contact time t_c, defined as the time during which the droplet is in apparent contact with the soap film (i.e. the time between impact and take-off), was measured for various We. As seen in figure 11(a),

$$t_c \simeq 1.86\tau_c. \tag{2.2}$$

The contact time t_c is proportional to the capillary time $\tau_c = \sqrt{m/\sigma}$ and independent of We. We note that these results have similarities with those reported by Courbin *et al.* (2006) for beads bouncing on elastic membranes and by Richard *et al.* (2002) for droplets bouncing on hydrophobic surfaces. In both cases, the contact time also increases with the mass of the bouncing particle. We note that the proportionality constant reported by Richard *et al.* (2002), 1.27, is significantly less than that observed in our experiments, 1.86. The observed independence of τ_c on We will be rationalized in § 4. The influence of film and drop viscosity on contact time is reported in Appendix A.

During each bounce, a droplet loses a fraction of its initial mechanical (kinetic plus gravitational) energy through viscous dissipation. In dimensionless terms, the Weber number is decreased by an amount ΔWe at each bounce owing to dissipation within the droplet, soap film or intervening air layer. The coefficient of restitution, specifically the ratio of take-off and landing speeds, is given by

$$\gamma = \sqrt{1 - \frac{\Delta We}{We}}. \tag{2.3}$$

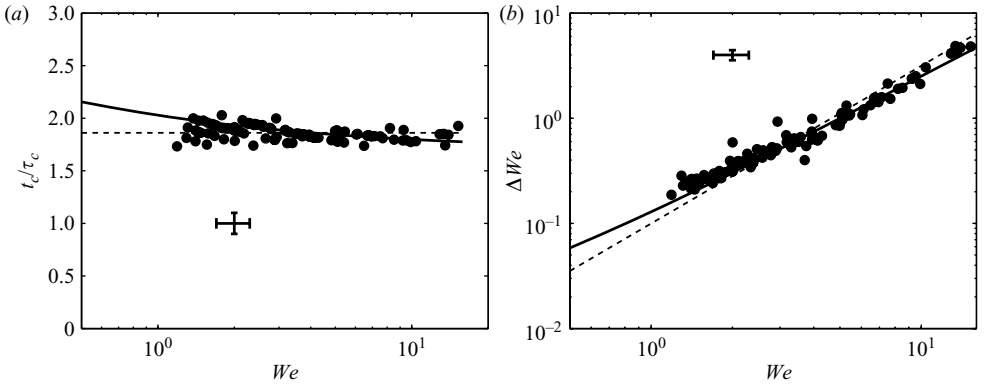

FIGURE 11. (*a*) Contact time t_c normalized by the capillary time $\tau_c = \sqrt{m/\sigma}$, and (*b*) difference in *We* before and after the bounce as a function of *We*, for $Oh = 0.015$. Dashed lines in (*a*) and (*b*) represent fits $t_c = 1.86\tau_c$ and $\Delta We = 0.087 We^{3/2}$, respectively. Solid lines were deduced by integrating (4.10) with $D = 8 \times 10^{-4}\,\mathrm{g\,cm^{-1}}$(best fit). The vertical error bar in (*a*), due to limitations in time resolution, is about $\pm 5\,\%$.

The dependence of ΔWe on *We* at $Oh = 0.015$ is reported in figure 11(*b*). The experimental data collapse onto a single curve corresponding to a power law close to

$$\Delta We \simeq 0.09 We^{3/2}. \tag{2.4}$$

The dissipation is markedly different from that observed by Richard & Quéré (2000) for droplets bouncing (at $We < 1$) on a hydrophobic surface, for which dissipation increases with impact speed at low impact speeds, but is roughly constant for high speeds. Energy dissipation will be discussed in § 4.1, where the observed scaling (2.4) will be rationalized. The dependence of the constant of proportionality on the film and drop viscosity is reported in Appendix A.

2.3. *Vibrating film*

On a stationary soap film, the *We* decreases at each bounce, until the droplet settles onto and ultimately merges into the film. To counter dissipative losses, a vertical vibration is applied to the frame of the soap film: energy is thus transferred from the frame to the film to the droplet. Provided the mechanical energy so supplied balances dissipative losses, the droplet is re-energized during impact and may bounce indefinitely. In the vibrating film experiments, $\beta = 20$ was held fixed.

The acceleration threshold Γ_C is the minimal acceleration $\Gamma = 4\pi^2 B f^2/g$ that can sustain periodic droplet trajectories. This threshold is measured for various forcing frequencies f and reported in figure 12. Results are markedly different from those describing droplets bouncing on a bath (Gilet *et al.* 2008). For frequencies $f < 55\,\mathrm{Hz}$, the threshold Γ_C is roughly constant (about 0.15 ± 0.04 g). When $f > 55\,\mathrm{Hz}$, bouncing droplets cannot be sustained. We note that this critical frequency corresponds to a period of 18 ms, a value roughly equal to the measured contact time. Our theoretical developments of § 3 and 4 will demonstrate that droplet bouncing can arise only if the system is forced at or below twice the natural frequency of the soap film.

A striking characteristic of droplet bouncing on soap films is the coexistence of multiple periodic solutions for given forcing parameters, f and Γ, or, in the

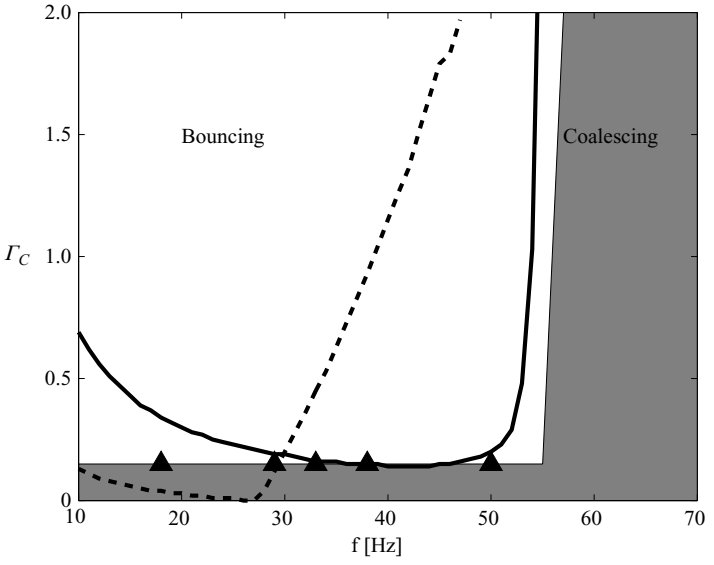

FIGURE 12. Threshold acceleration for bouncing, Γ_C, as a function of the forcing frequency f. Triangles (▲) represent experimental data. For a given frequency, a droplet was released onto a film vibrating at $\Gamma > \Gamma_C$; subsequently, Γ was decreased until the droplet coalesced. The experiment was repeated several times to capture both modes (1,1) and (2,1): the minimum measured value of Γ corresponds to the threshold reported by triangles. When forcing parameters (Γ, f) are located inside the shaded area, no periodic bouncing is observed and the droplet coalesces. Solid and dashed lines represent thresholds computed by solving (4.14) numerically. The solid and dashed curves correspond to the thresholds of modes (2,1) and (1,1), respectively. The lower threshold roughly corresponds to our experimental data.

parlance of dynamical systems theory, multi-periodicity. Figure 13 represents different trajectories of droplets achieved with the same forcing. The image is made by extracting a thin vertical slice along the droplet centreline from each frame of the movie, then placing those slices side by side. Bouncing modes are denoted by two integers (m, n) such that one period of the trajectory corresponds to m forcing periods and n bounces of the droplet. For example, modes (1,1), (2,1) and (3,1) are displayed in figure 13(a–c). All these solutions are observed to be stable, at least during the 8 seconds of recording corresponding to 240 forcing periods. Depending on initial conditions, specifically the impact speed and phase, the droplet locks onto one particular mode (figure 13d). Note that the amplitude of the jumps experienced by modes (2,1) and (3,1) is much larger than the forcing amplitude. Weber numbers at impact are about 0.06, 1.5 and 3.9 for modes (1,1), (2,1) and (3,1), respectively. According to (2.4), with each bounce these modes lose kinetic energy such that ΔWe is approximately 10^{-3}, 0.16 and 0.67, respectively. For periodic solutions, this energy loss has to be perfectly balanced by the energy input from the forcing. In § 4.2, we shall demonstrate that the same forcing can deliver three different amounts of energy according to the impact phase of the droplet.

Finally, we observed more complex periodic bouncing states, where the periodicity appears only after several jumps ($n > 1$). An example is provided in figure 14(a), where a droplet bounces on a soap film vibrated at 33 Hz and 0.7 g. The mode (3,3) is characterized by three successive jumps of different amplitude. At higher accelerations, a period-doubling transition may occur spontaneously (at fixed forcing

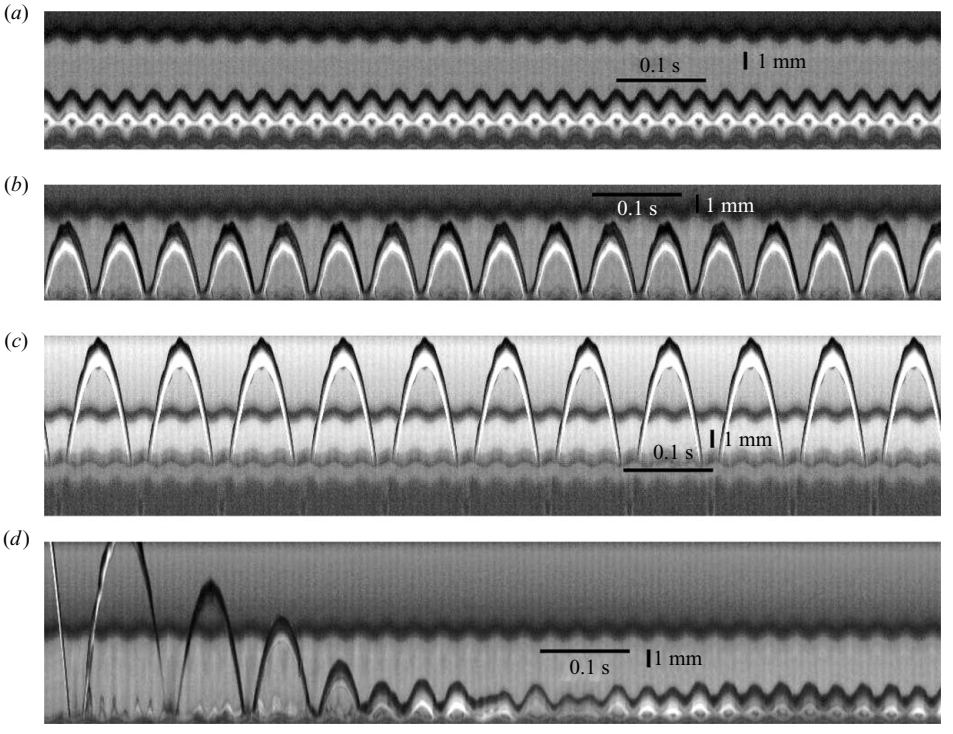

FIGURE 13. Multi-periodicity in the bouncing states: multiple solutions arise for the same forcing ($f = 33$ Hz, $\Gamma = 0.6$). The vertical trajectory of the droplet is displayed as a function of time. (*a*) Mode (1,1) at $We \simeq 0.06$. (*b*) Mode (2,1) at $We \simeq 1.5$. (*c*) Mode (3,1) at $We \simeq 3.9$. The dark low-amplitude oscillation at the top of those pictures represents the vertical motion of the ring to which the soap film is pinned. (*d*) A transient period arises before the drop locks onto a particular solution, here the (1,1) mode.

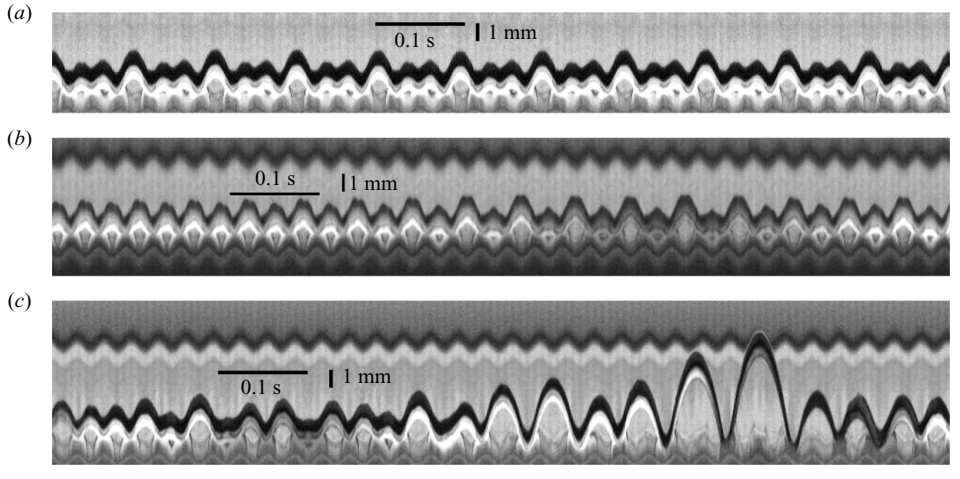

FIGURE 14. Complex bouncing modes. The vertical trajectory of the droplet is displayed as a function of time. (*a*) A periodic mode (3,3) consists of three successive jumps ($f = 33$ Hz, $\Gamma = 0.7$). $We = 0.015$, 0.074 and 0.3 during the small, the medium and the large jumps, respectively. (*b*) A period-doubling transition, from mode (1,1) to mode (2,2), observed at $f = 33$ Hz, $\Gamma = 1.2$. (*c*) A chaotic bouncing trajectory observed at $f = 33$ Hz, $\Gamma = 1.1$.

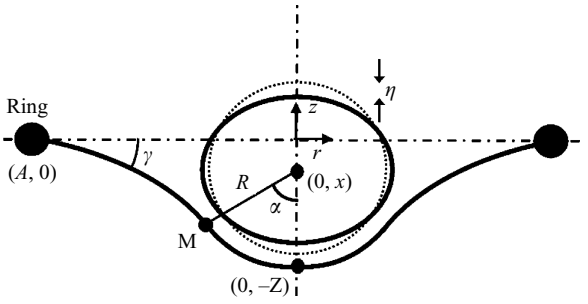

FIGURE 15. Hypothetical shape for the soap film: the region of curvature $2/R$ below the droplet matches onto an exterior region of zero curvature at the point M corresponding to an angle α. The soap film is pinned at $(r, z) = (A, 0)$, while its point of maximum centreline deflection is $(0, -Z)$. The centre of mass of the droplet is at $(0, x)$, and its vertical deflexion is denoted by η.

parameters), transforming a mode (1,1) into a mode (2,2) as seen in figure 14(*b*). Chaotic trajectories are also observed (figure 14*c*), with episodic periods of high-amplitude bouncing. We note that the chaotic bouncing is usually unstable and the air film ultimately breaks, typically after a particularly vigorous impact.

3. Modelling the soap film as a nonlinear spring

3.1. *Soap film shape*

We proceed by rationalizing the bouncing-to-crossing transition. We first model the shape of the soap film, and so deduce a relation between the drop position and the force generated by the soap film. We note that the soap film reacts to the external forcing associated with the impacting droplet at a time scale determined by the speed of capillary waves on the soap film, $V_w \sim \sqrt{\sigma/(\rho\delta)}$ (LeGrand-Piteira *et al.* 2006). For a film of thickness $\delta = 1\,\mu$m, the wave speed, $V_w \sim 500$ cm s^{-1}, is approximately 10 times larger than the characteristic droplet impact speed. The soap film thus adjusts rapidly to the applied forcing, the information being transmitted by capillary waves (Boudaoud, Couder & Ben Amar 1999). For the relatively low impact speeds considered in our study, the film shape may thus be described as quasi-static.

The soap film deforms in response to the impinging droplet. We assume that the droplet remains roughly spherical and that, near the droplet, the soap film is a spherical cap lying tangent to the droplet with constant mean curvature $2/R$. Beyond the droplet, the soap film has zero curvature since the air pressure is atmospheric on either side (figure 15). The only non-planar axisymmetric surface that has zero mean curvature is the catenoid

$$\frac{z}{r_0} = -\operatorname{acosh}\left(\frac{A}{r_0}\right) \pm \operatorname{acosh}\left(\frac{r}{r_0}\right), \tag{3.1}$$

where r_0 is the minimum radius of the catenoid. We must match this catenoid to the spherical cap at a point prescribed by the angle α: $r_0/R = \sin^2\alpha$. The maximum vertical deformation Z of the soap film may be expressed as a function of α through

$$\frac{Z}{R} = 1 - \cos\alpha + \sin^2\alpha\left[\operatorname{acosh}\left(\frac{1}{\sin\gamma}\right) - \operatorname{sign}(\cos\alpha)\operatorname{acosh}\left(\frac{1}{\sin\alpha}\right)\right], \tag{3.2}$$

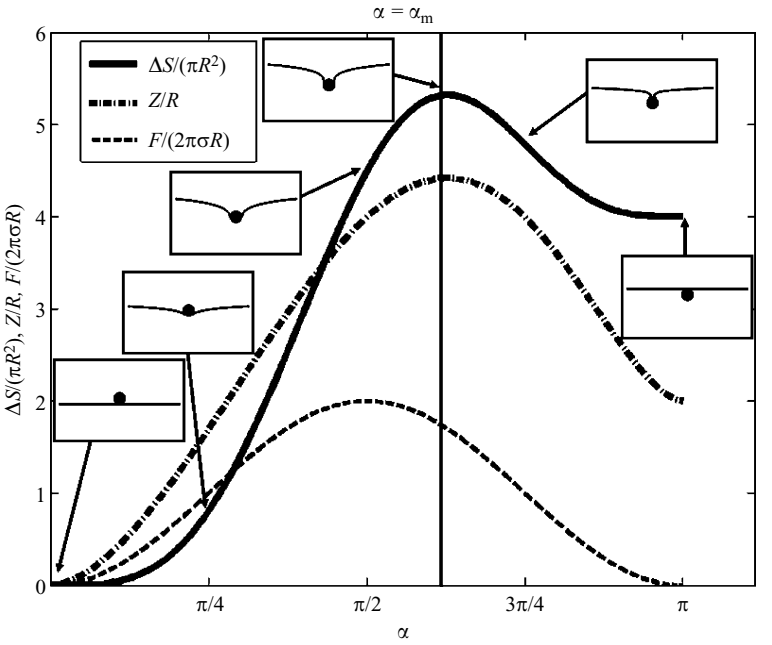

FIGURE 16. Variation of $\Delta S/(\pi R^2)$, Z/R and $F/(2\pi\sigma R)$ with α, for $\beta = A/R = 10$. Insets represent the shape of the film for different values of α.

where $\sin\gamma = r_0/A = (\sin^2\alpha)/\beta$. The anomalous surface generated by the film deformation, ΔS, is given by

$$\frac{\Delta S}{\pi R^2} = (1-\cos\alpha)^2(2+\cos\alpha) - \frac{\sin^4\alpha}{1+\cos\gamma} + \sin^4\alpha\left[\operatorname{acosh}\left(\frac{1}{\sin\gamma}\right) - \operatorname{sign}(\cos\alpha)\operatorname{acosh}\left(\frac{1}{\sin\alpha}\right)\right]. \quad (3.3)$$

The vertical force F required to produce a vertical displacement Z is given by

$$\frac{F}{2\sigma\pi R} = \frac{\partial_\alpha \Delta S/(\pi R^2)}{\partial_\alpha Z/R} = 2\sin^2\alpha. \quad (3.4)$$

Of course, this force is obtained more easily by integrating the vertical component of the surface tension over the circle formed by revolving the point of matching M about the vertical axis $r = 0$.

The dependence on α of $\Delta S/(\pi R^2)$, Z/R and $F/(2\pi\sigma R)$ is illustrated in figure 16 for $\beta = 10$. The anomalous surface ΔS reaches a maximum for a critical angle $\alpha_m \simeq 5\pi/8$. For $\alpha < \alpha_m$, the system tends to the $\alpha = 0$ state (droplet above the soap film), while for $\alpha > \alpha_m$ it tends to the $\alpha = \pi$ state (droplet fully enclosed by the soap film). The maximum deflection $Z/R \simeq 4.4$ is also reached for $\alpha = \alpha_m$. The force F exerted by the soap film on the droplet remains directed upwards, whatever the value of α. The maximum force generated by the soap film, $F = 4\pi\sigma R$, occurs when $\alpha = \pi/2$. The force is represented as a function of the maximum centreline deflection Z in figure 17*a*. Four distinct regimes are apparent.

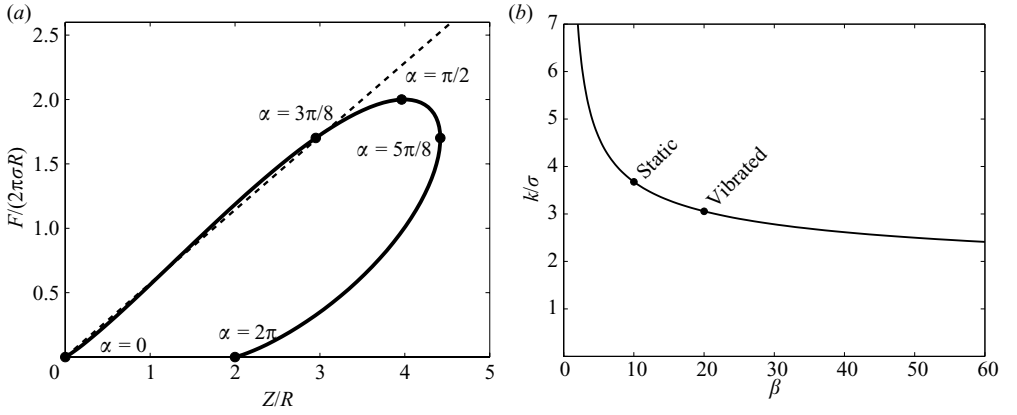

FIGURE 17. (*a*) Theoretically predicted force–displacement curve for a spherical drop impinging on a soap film. The solid line represents the variation of the force $F/(2\pi\sigma R)$ with respect to the maximum film deflection Z/R for $\beta = 10$. The dashed line represents the linear spring approximation (3.5). (*b*) The dependence of the spring constant k on β. Values appropriate for our static ($\beta = 10$) and vibrating ($\beta = 20$) film experiments are indicated.

When $0 < Z < 3$ ($0 < \alpha < 3\pi/8$), the soap film reacts like a spring, exerting a force that grows roughly linearly with the deformation:

$$F = kZ, \tag{3.5}$$

where the spring constant $k = (8\pi/7)\sigma$. When $3 < Z < 4$ ($3\pi/8 < \alpha < \pi/2$), the spring law becomes nonlinear as the force saturates. The stiffness vanishes when $\alpha \to \pi/2$. When $4 < Z < 4.4$ ($\pi/2 < \alpha < \alpha_m$), the stiffness is negative: increasing the deformation results in decreasing force. The stiffness diverges when $\alpha \to \alpha_m$ and the system switches equilibrium states. When $\alpha > \alpha_m$, Z decreases towards 2 and the stiffness is again positive. Here, the system tends towards the $\alpha = \pi$ configuration, where the droplet is wrapped by the film. We note that for $\alpha > \alpha_m$, the film shape is poorly described by the model: the last three frames of figure 4 clearly indicate that the film does not wrap the drop as it passes through. Nevertheless, as we shall see, the quasi-static film model provides an excellent description of the bouncing states, for which $\alpha < \alpha_m$.

It is important to note that the spring constant k depends on the impact geometry, specifically on $\beta = A/R$. The dependence of k/σ on β is illustrated in figure 17*b*. As β increases from 10 to 20, the values appropriate for our static and vibrating film experiments, respectively, k decreases from $8\pi/7$ to $24\pi/25$.

3.2. *Comparison with experiments*

In figure 18, the shape of the soap film is measured experimentally and compared to the model shape of catenoid plus spherical cap. The agreement is excellent, particularly for the catenoidal portion. We note that the modelling of the film below the droplet might be slightly improved by considering a spheroidal instead of a spherical cap. However, calculations become much more complicated, and do not yield further insight into the film dynamics. The relation (3.2) between the angle of matching α and the maximum deformation Z is examined in figure 19(*a*). Experimental data are gathered from a full cycle of a droplet in a bouncing state. The hysteresis is very weak: the deformation is roughly the same whether the drop is

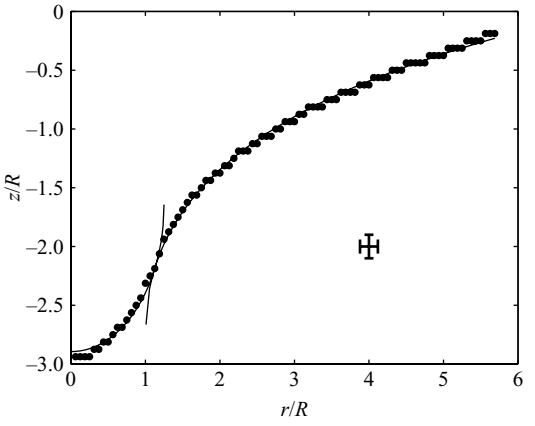

FIGURE 18. Observed shape of the soap film (dots) caused by impact at $We = 9.7$. The thick solid curves represent the 'sphere plus catenoid' model: the film has curvature $2/R$ beneath the drop and zero beyond.

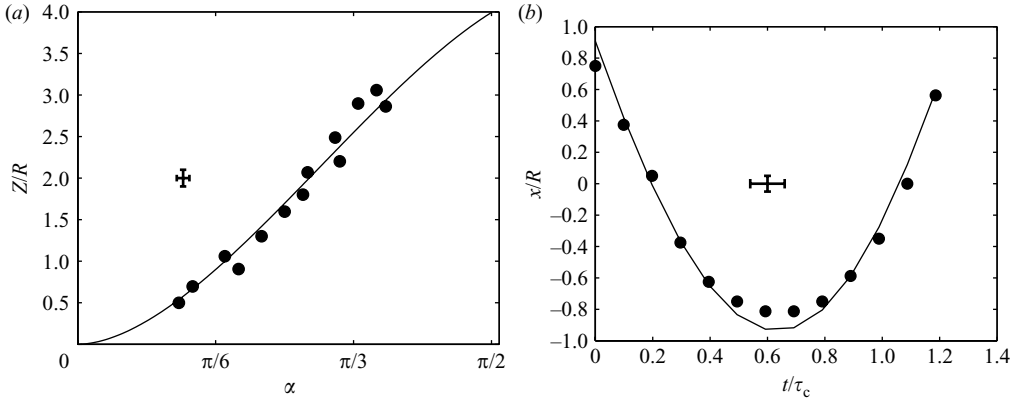

FIGURE 19. Impact at $We = 9.7$ (a) Maximum vertical deflection of the film as a function of α, the slope at the matching point. (b) Trajectory of the droplet's centre of mass, x. The solid line represents the trajectory reconstructed from the model (3.6), in which gravity and the force exerted by the soap film are taken into account.

rising or falling, which lends added credibility to our quasi-static description of the soap film.

We next check the force predicted by (3.4). Experimentally, we measure the trajectory of the droplet's centre of mass during one bounce. Assuming that the air layer intervening film and drop serves only to communicate to the droplet the force exerted by the soap film, the height x of the droplet's centre of mass must evolve according to

$$m\ddot{x} = -mg + F, \tag{3.6}$$

where m is the mass of the droplet, and F is the force exerted by the film as deduced from (3.4). The radial position and slope of the interface at the matching point are measured through R and α (figure 15) from each recorded frame. The concomitant film-induced force F is integrated twice, and the drop trajectory reconstructed. The trajectory so deduced compares favourably with that measured (figure 19b).

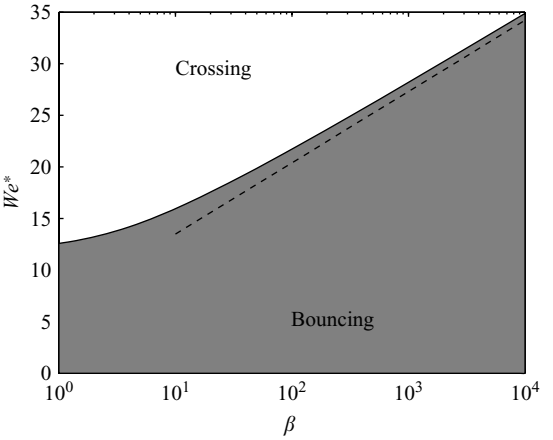

FIGURE 20. Critical Weber number We^* for the bouncing-to-crossing transition, as a function of the ratio $\beta = A/R$ between the soap film and the droplet radii. The solid line corresponds to (3.8), and the dashed line to the asymptotic behaviour $We^* \sim 4.5 + 3\ln(2\beta)$ relevant for $\beta \gg 1$.

For $Z < 3$, the force exerted by the film is linear in Z, as in (3.5). The film thus behaves like a linear spring with spring constant $k = (8\pi/7)\sigma$, and natural frequency

$$f = \frac{1}{2\pi}\sqrt{\frac{k}{m}} = 0.3/\tau_c \simeq 30 \text{ Hz}. \tag{3.7}$$

One expects the contact time to be approximately half a period of oscillation of the soap film, i.e. $t_c = 1.66\tau_c$, which is in good agreement with the experimental results reported in figure 11(a) and Appendix A. The agreement between the experiments and model predictions for the bouncing case suggests that, to leading order, the action of the film is well described by the force–displacement relation defined in figure 17a.

Finally, we apply this quasi-static model for the film shape to estimate the minimum Weber number, We^*, required for a droplet to pass through the soap film. Supposing that the whole initial kinetic energy is converted into surface energy of the film, the energy balance is written $(2\pi/3)\rho R^3 U^2 = 2\sigma \max(\Delta S)$, so

$$We^* = 3\frac{\max(\Delta S)}{\pi R^2}. \tag{3.8}$$

Figure 20 illustrates the dependence of this critical Weber number We^* on the film size $\beta = A/R$. According to (3.3), we expect We^* to tend asymptotically to $4.5 + 3\ln(2\beta)$ in the large film limit, $\beta \to \infty$; however, we note that this limit is likely to be poorly described by our quasi-static model, as the influence of the finite wave speed will ultimately become important on sufficiently large films. In our experiments, the soap film has a radius of $A = 0.8$ cm and corresponding $\beta = 10$; we thus anticipate a critical $We^* = 16$. This value is in good agreement with the experiments reported in figure 10. We note that the prediction (3.8) neglects energy dissipated during impact as well as the droplet deformation. Nevertheless, it does provide a good leading-order criterion for droplet breakthrough. We further note that the relative increase in the soap film surface area is less than 6 % when $We = We^* = 16$, and the mean film thickness necessarily decreases proportionally.

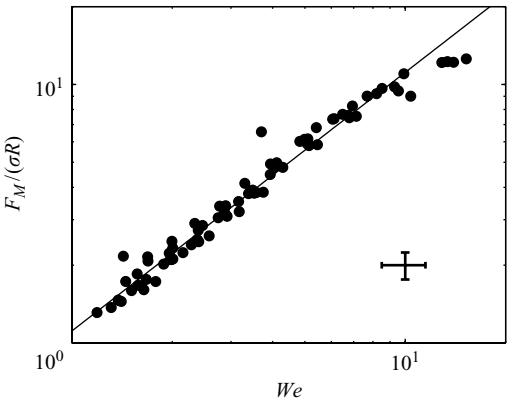

FIGURE 21. Dependence on We of the maximum force F_M applied by the soap film on the droplet, for $Oh = 0.015$, $\beta = 10$. The maximum deflection Z is measured experimentally, and F_M is computed according to (3.2) and (3.4). The solid line corresponds to $F_M/(\sigma R) = 1.11We$.

4. Theoretical model

We proceed by developing a simple theoretical model to describe bouncing on a soap film. Our model has similar features to those developed by Okumura *et al.* (2003), Legendre *et al.* (2005), Biance *et al.* (2006) and Gilet *et al.* (2008) to describe droplet bouncing in various scenarios. The centre of mass of the droplet x evolves according to

$$m\ddot{x} = F(Z) + mg[\Gamma\cos(2\pi ft + \phi) - 1], \tag{4.1}$$

where $F(Z)$ is the force exerted by the soap film with centreline deflection Z. Since Newton's law is expressed in a frame moving with the vibrating film, a fictitious inertial force $mg\Gamma\cos(2\pi ft + \phi)$ is included. If η denotes the vertical deformation of the droplet (figure 15), we can write $x = -Z + R + \eta$. Equation (4.1) can then be recast in terms of energy as

$$\frac{\mathrm{d}}{\mathrm{d}t}\left[\frac{m\dot{x}^2}{2} + mgx + E(Z)\right] = F(Z)\dot{\eta} + mg\Gamma\dot{x}\cos(2\pi ft + \phi), \tag{4.2}$$

where $E(Z)$ is the surface energy stored in the soap film, so that $\mathrm{d}E(Z)/\mathrm{d}Z = F(Z)$.

4.1. *Stationary film*

We first consider the case of a stationary film ($\Gamma = 0$). The only remaining non-conservative term in (4.2) is $F(Z)\dot{\eta}$, the work done by the soap film in deforming the droplet. This term describes the transfer of energy between the translational and vibrational motions of the droplet. The total energy removed in this fashion during impact necessarily scales as $F\dot{\eta}t_c$. We proceed by rationalizing the scaling observed in figure 11(b), then exploiting it in simplifying our model.

The maximum centreline deflection of the soap film, Z, was measured for various We. If $Z < 4$ (i.e. $\alpha < \pi/2$), the maximum force F_M exerted by the soap film occurs at the point of maximum deflection and can be calculated from (3.2) and (3.4). As shown in figure 21,

$$\frac{F_M}{\sigma R} \simeq 1.11We. \tag{4.3}$$

The maximum force is linearly proportional to We, a result that may be understood by considering that the incoming kinetic energy $mU^2/2$ is eventually converted into surface energy $\sim F_M R$. The influence of droplet and film viscosity on the peak force F_M is reported in Appendix A.

The droplet deformation rate during impact $\dot{\eta}$ scales as η_M/τ_c, where η_M is the maximum droplet deformation. As seen in figure 3, the droplet reacts rapidly to the impact: it is already highly compressed by the time the soap film begins to deform. Indeed, the natural frequency of the soap film is given by (3.7), while according to Landau & Lifchitz (1959) the natural frequency of the mode 2 droplet oscillation is

$$f_d = \frac{1}{2\pi}\sqrt{\frac{32\pi\sigma}{3m}} = \frac{0.92}{\tau_c} \simeq 90 \text{ Hz}, \tag{4.4}$$

so the droplet reacts three times faster than the soap film. For an experiment at $We \simeq 9$ corresponding to a kinetic energy $K \simeq 2.60$ erg, the maximum drop deformation is estimated to be $\eta_M \simeq 0.033$ cm, so that $\eta_M/R \sim 0.41$. The corresponding energy in the mode 2 drop vibration is calculated in Appendix B and found to be

$$E_d \simeq 8\pi\sigma\eta_M^2/5 \simeq 0.13 \text{ erg}, \tag{4.5}$$

which represents a fraction $\Lambda \simeq 5\,\%$ of the initial kinetic energy $K = (1/2)mU^2$. This lost energy at impact cannot account for the characteristic value $\Delta We/We \sim 0.25$ observed in figure 11(b), from which we infer that some additional energy is transferred after impact. Substituting $E_d = \Lambda K$ into (4.5) yields a scaling for η_M

$$\left(\frac{\eta_M}{R}\right)^2 \simeq \frac{5}{8\pi\sigma R^2}\Lambda K = \frac{5}{12}\Lambda We. \tag{4.6}$$

We note that this scaling is similar to that observed by Clanet *et al.* (2004) for droplets striking a hydrophobic surface. Indeed, they reported that $a/R \sim We^{1/4}$, where a is the maximum horizontal radius of the spheroidal droplet, so that $1 + \eta_M/R \sim We^{1/2}$.

Equations (2.2), (4.3) and (4.6) together yield

$$\begin{aligned}\Delta We &= \frac{3}{2\pi\sigma R^2}\Delta K = \frac{3}{2\pi\sigma R^2}\int_0^{t_c} F\dot{\eta}\,\mathrm{d}t \\ &\sim \frac{3(1.11\sigma R We)(\sqrt{5\Lambda We/12}\ R/\tau_c)(1.86\tau_c)}{2\pi\sigma R^2} = 0.63\Lambda^{1/2}We^{3/2}.\end{aligned} \tag{4.7}$$

For $\Lambda = 5\,\%$, we thus obtain

$$\Delta We \approx 0.14 We^{3/2}, \tag{4.8}$$

which is close to the observed scaling (2.4). While the coefficient deduced (0.14) is 50 % higher than that observed (0.087), this estimate has not taken into account the variations of the sign of $F\dot{\eta}$ over the integration period. Nevertheless, since t_c/τ_c is independent of We, it is reasonable to suppose that the time correlation of F and $\dot{\eta}$ remains unchanged with increasing We, which lends further credibility to this scaling.

Equation (4.2) cannot be solved unless an evolution equation for the drop deformation η is written. Instead, for the sake of mathematical simplicity, we model the dissipation term $F(Z)\dot{\eta}$ as a function of $\dot{Z}$, specifically $-DH(Z)|\dot{Z}|^3$, where $H(Z)$ is the Heavyside function, and D is a constant. The dissipation is zero when $Z < 0$, but is negative definite and scales as $We^{3/2}$ when $Z > 0$. Note that since F_M grows

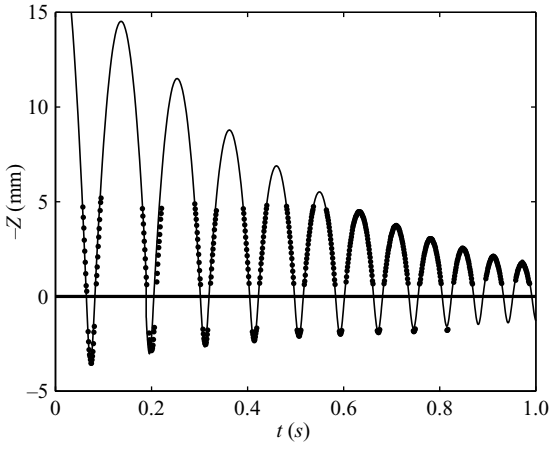

FIGURE 22. Observed (dots) and simulated (solid line) trajectories of a droplet released at $We = 15.24$ and bouncing on a stationary soap film ($\beta = 10$). Model parameters are $m = 2.25 \times 10^{-3}$ g, $k = (8\pi/7)\sigma = 77\,\mathrm{dyn\,cm^{-1}}$ and $D = 8 \times 10^{-4}\,\mathrm{g\,cm^{-1}}$(best fit value inferred from figure 11). Experimental data could only be obtained in the apparent field of view, that was partially obscured by the frame of the soap film and also limited from above.

as $We \sim U^2$, we expect the work rate to scale as $U^3 \sim |\dot{Z}|^3$. We further simplify the system by assuming that $|\eta| \ll |Z|$: the droplet deformation is much smaller than the amplitude of vertical motion, so that $x \simeq R - Z$. Finally, consistent with (3.5), we assume that the soap film has a linear force–displacement law $F(Z) = H(Z)kZ$, where $k = (8\pi/7)\sigma$ on our stationary film ($\beta = 10$), and $k = (24\pi/25)\sigma$ on our vibrating film ($\beta = 20$). In the absence of forcing, $\Gamma = 0$, we thus obtain

$$\frac{\mathrm{d}}{\mathrm{d}t}\left[\frac{m\dot{Z}^2}{2} - mgZ + H(Z)\frac{kZ^2}{2}\right] = -DH(Z)|\dot{Z}|^3, \tag{4.9}$$

so

$$m\ddot{Z} = mg - kZH(Z) - DH(Z)\dot{Z}|\dot{Z}| \ . \tag{4.10}$$

The constant $D = 8 \times 10^{-4}\,\mathrm{g\,cm^{-1}}$ is determined by fitting the solutions of (4.10) to the experimental data in figure 11(*b*). We note that the results from (4.10) with the D value so deduced represent an improvement over the scaling law (2.4). The predicted contact time t_c/τ_c is also in good agreement with experimental data reported in figure 11(*a*). As seen in figure 22, the model produces a remarkably accurate picture of the damped bouncing on a stationary film. The various sources of dissipation in the film–air-drop system are considered in Appendix C.

4.2. *Forced film*

By adding the forcing term to (4.9) and (4.10), we can model the dynamics of a droplet on a vibrating film in terms of a single second-order ordinary differential equation,

$$m\ddot{Z} = mg - kZH(Z) - DH(Z)\dot{Z}|\dot{Z}| - mg\Gamma\cos(2\pi ft + \phi). \tag{4.11}$$

Defining non-dimensional variables

$$y = \frac{-kZ}{mg}; \quad \tau = \sqrt{\frac{k}{m}}t; \quad V^2 = \frac{kU^2}{mg^2}; \quad \Psi = \frac{Dg}{k}; \quad \omega = \Omega\sqrt{\frac{\sigma}{k}} = 2\pi f\sqrt{\frac{m}{k}} \tag{4.12}$$

yields

$$\ddot{y} + H(-y)y + 1 = -H(-y)\Psi|\dot{y}|\dot{y} + \Gamma\cos(\omega\tau + \phi), \tag{4.13}$$

which may be solved subject to initial conditions $y(0) = 0$ and $\dot{y}(0) = -V$ at impact. This second-order non-autonomous equation may be written as a system of three first-order autonomous equations by defining $\theta(\tau) = \mathrm{mod}(\omega\tau + \phi, 2\pi)$ as a third variable:

$$\left.\begin{aligned} \frac{\mathrm{d}y}{\mathrm{d}\tau} &= \dot{y}, \\ \frac{\mathrm{d}\dot{y}}{\mathrm{d}\tau} &= -1 - H(-y)[y + \Psi|\dot{y}|\dot{y}] + \Gamma\cos\theta, \\ \frac{\mathrm{d}\theta}{\mathrm{d}\tau} &= \omega. \end{aligned}\right\} \tag{4.14}$$

We note that the system (4.14) is similar to that arising from the Duffing equation, that describes the inelastic bouncing ball (Kowalik, Franaszek & Pieranski 1988; Mehta & Luck 1990) and the vertically oscillated pendulum (McLaughlin 1981). We thus anticipate that it may support chaotic solutions.

The system of (4.14) was integrated from a variety of initial conditions $(y, \dot{y}, \theta) = (0, -V, \phi)$. In our experiments (figure 13*a–c*), multi-periodicity is observed: different periodic solutions arise (figure 23) for a single pair of forcing parameters (Γ, ω), each solution corresponding to a different limit cycle in the $(y, \dot{y}, \theta)$ space. Take-off and landing phases are measured in the experiments, and superposed on the model solutions in figure 23(*b–d*). The phases of take-off and landing are in good agreement. Note that in figure 23(*a*), the droplet in the high-energy mode (3,1) lands before that in low-energy mode (1,1), thereby increasing the amount of energy extracted during impact.

The model also reproduces complex modes such as those reported in figure 14. In figure 24, measured phases of landing and take-off are compared to the model solution. Although the agreement is good, these complex modes are not observed at precisely the same forcing parameters as in the experiments. For example, modes (3,3) and (2,2) are observed, respectively, at $\Gamma = 0.85$ and $\Gamma = 1.5$ in the model and at $\Gamma = 0.7$ and $\Gamma = 1.2$ in the experiments.

Many other complex periodic solutions are generated by the model for different forcing parameters (Γ, ω) and initial conditions (V, ϕ). Some of these modes arising at a forcing frequency $\omega = 1.21$ are illustrated in figure 25. In figure 25(*a*), the solution is displayed for $\Gamma = 0.05 < \Gamma_C$. Below the acceleration threshold Γ_C, periodic bouncing cannot be sustained: the intervening air layer thins and the droplet eventually coalesces. Two distinct complex periodic modes may arise at $\Gamma = 0.65$ (figure 25*b–c*), and chaotic motion emerges at $\Gamma = 1.82$ (figure 25*d*).

In figure 26, a periodic solution (2, 1) arising at $\omega = 1.21$, $\Gamma = 1$ is compared to a chaotic solution arising at $\omega = 1.21$, $\Gamma = 1.82$. Specifically, we plot phase-plane trajectories $(y, \dot{y})$, power spectra of the trajectory $y(t)$ and Lyapunov exponents deduced by calculating the rate of exponential divergence of two initially adjacent points in phase space. For $\Gamma = 1$, the phase plane reveals a stable limit cycle: the power spectrum is discrete and the Lyapunov exponent is negative. For $\Gamma = 1.82$, the phase plane reveals a chaotic attractor: the power spectrum is full and the Lyapunov exponent positive. The latter indicates the sensitivity on initial conditions that is the hallmark of chaos (Lorenz 1963).

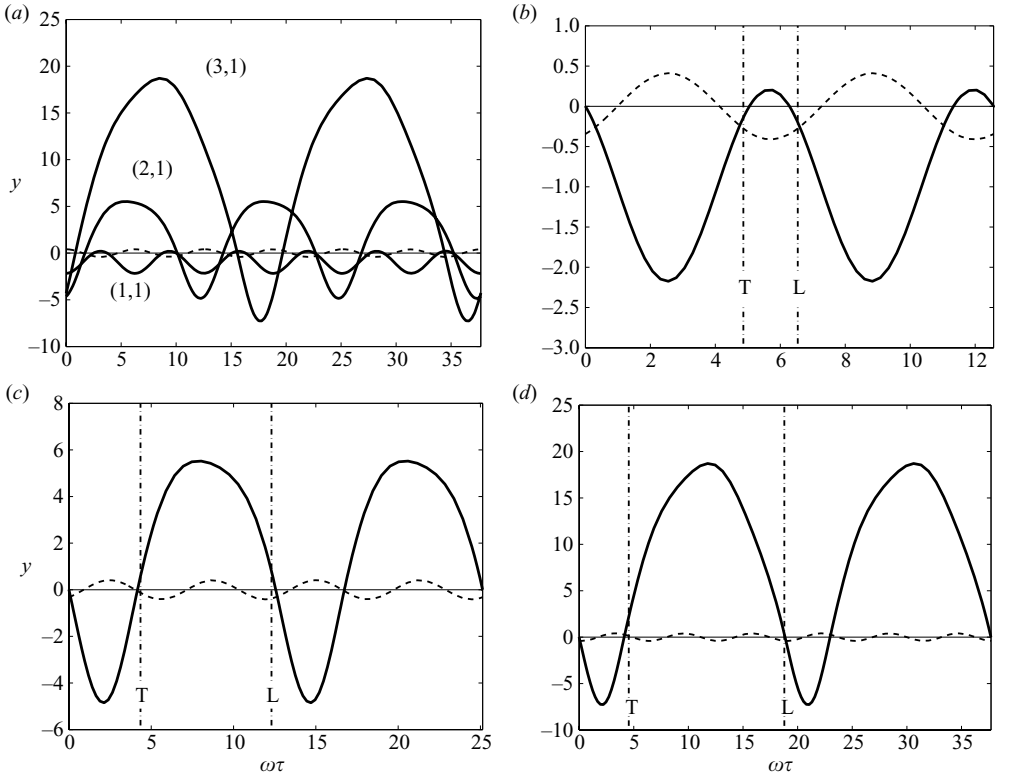

FIGURE 23. Multi-periodicity of bouncing modes at $f = 33\,\mathrm{Hz}$ ($\omega = 1.21$) and $\Gamma = 0.6$, corresponding to the forcing parameters of the trajectories reported in figure 13. Solid lines correspond to trajectories $y(t)$ computed from (4.14); dashed lines correspond to the film motion; vertical dash–dotted lines represent the landing (L) and take-off (T) phases measured experimentally (figure 13). (*a*) Modes (1,1), (2,1) and (3,1). (*b*) Mode (1,1). (*c*) Mode (2,1). (*d*) Mode (3,1). Note that the free-fall portion of the trajectory is not a parabola since $y(t)$ is the position of the droplet in a frame that moves with the vibrating soap film.

We proceed by solving (4.14) with $\omega = 1.21$ fixed for various accelerations $\Gamma \in [0, 2]$ to develop a bifurcation diagram of our system. For each Γ, simulations are run with different initial conditions (V, ϕ). The transient is removed from the results, and the impact speed measured at each bounce. Recall that a mode (m, n) is represented by n different branches corresponding to n different bounces. For practical purposes, only the principal bouncing modes are presented in figure 27. Several complex bifurcation events appear on the bifurcation diagram, analysis of which is beyond the scope of this paper. Nevertheless, we note some important features. For $\Gamma < 0.18$, no periodic bouncing is possible. $\Gamma_C^{(2,1)} = 0.18$ corresponds to the lower bouncing threshold, at which mode (2, 1) appears. At the upper bouncing threshold, $\Gamma_C^{(1,1)} = 0.47$, the static solution completely disappears and transforms into a periodic bouncing mode (1, 1). Both thresholds are computed for various forcing frequencies ω (figure 12), the lower of which is in good agreement with experiments. In particular, the threshold remains roughly constant and less than 0.2 until $f = 55\,\mathrm{Hz}$; thereafter, it increases drastically, consistent with the observed absence of bouncing for $f \gtrsim 55\,\mathrm{Hz}$ ($\omega \gtrsim 2$). We note that the minimum in the upper threshold curve corresponds to the resonant frequency of the soap film, 30 Hz in our experiments, as defined in (3.7).

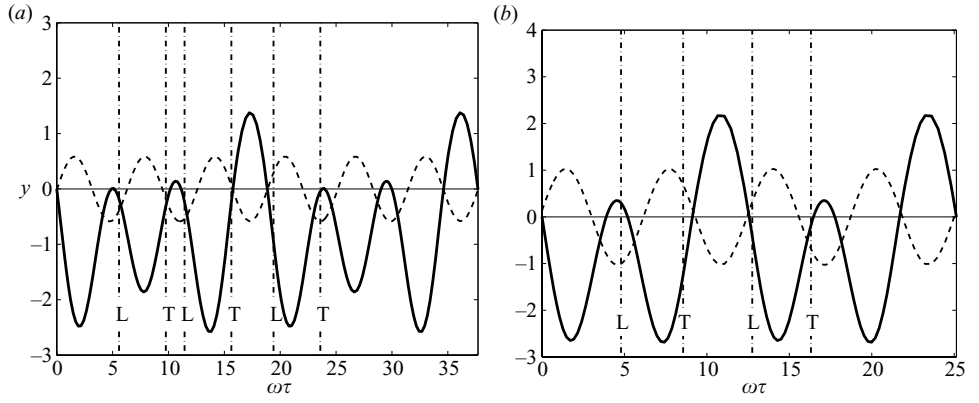

FIGURE 24. (*a*) Mode (3,3) observed at $(\Gamma, \omega) = (0.8545, 1.21)$ and (*b*) mode (2,2) observed at $(\Gamma, \omega) = (1.5, 1.21)$. In both cases, solid lines correspond to trajectories $y(t)$ in the frame of the film, dashed lines correspond to the film motion and dash–dotted lines represent the landing (L) and take-off (T) phases measured experimentally at $(\Gamma, \omega) = (0.7, 1.21)$ and $(\Gamma, \omega) = (1.2, 1.21)$, respectively.

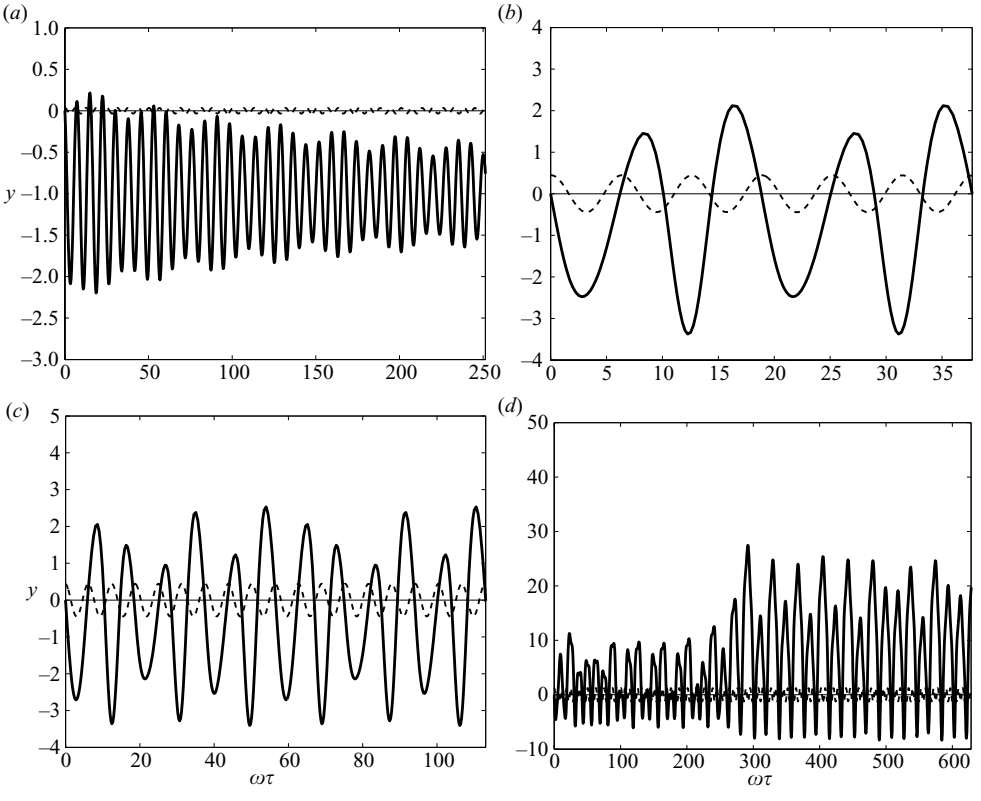

FIGURE 25. Other modes produced by integrating (4.14) for $\omega = 1.21$. (*a*) No bouncing at $\Gamma = 0.05$. (*b*) Mode (3,2) at $\Gamma = 0.65$. (*c*) Mode (9,6) at $\Gamma = 0.65$. (*d*) Chaotic motion at $\Gamma = 1.82$. The transition to chaos occurs via a cascade of period-doubling events, each of which transforms a mode (m, n) into a mode $(2m, 2n)$. The solid line corresponds to the trajectory $y(t)$ in the frame of the ring, and the dashed line to the ring motion.

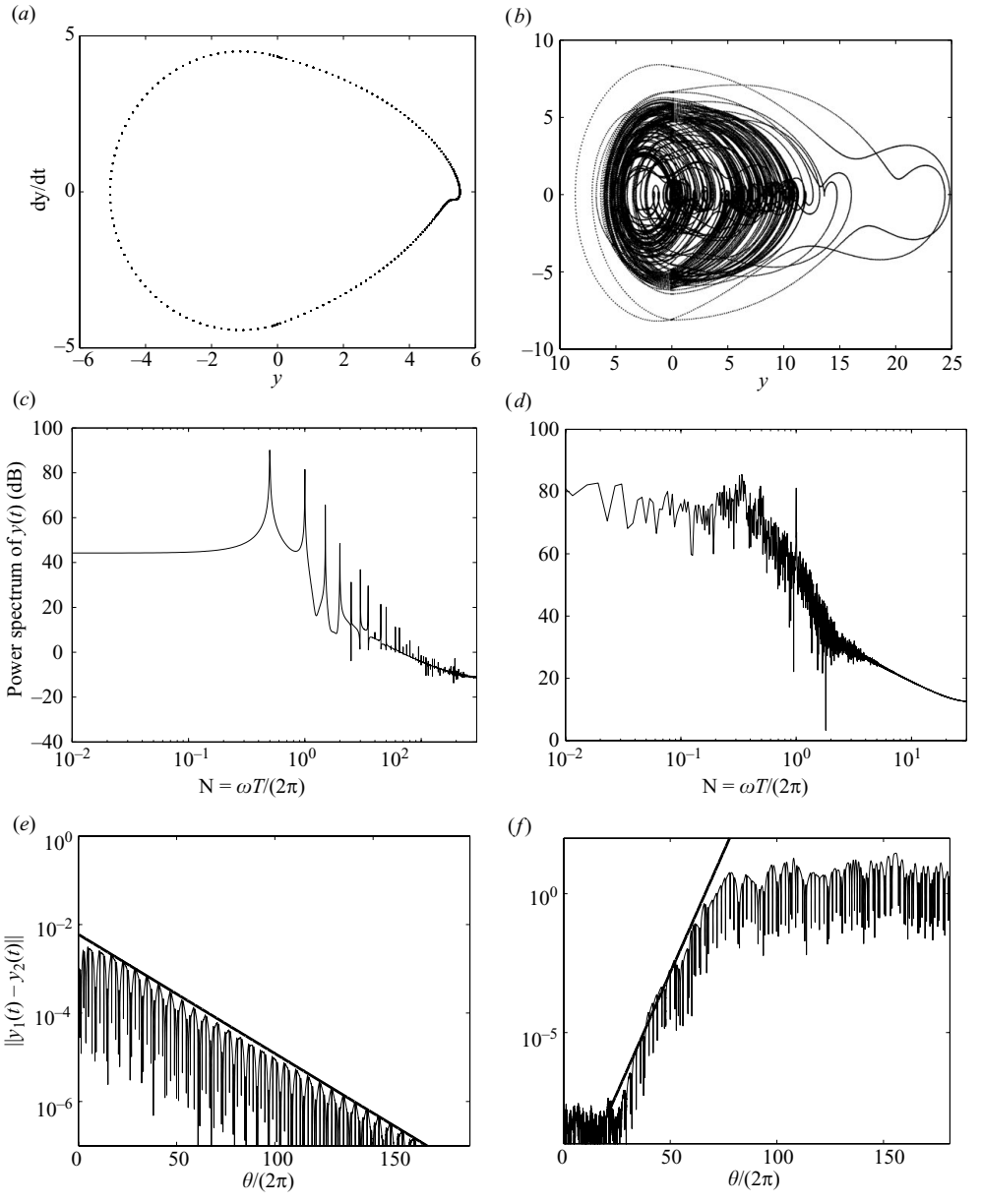

FIGURE 26. Periodic and chaotic solutions for $\omega = 1.21$. (*a*) Limit cycle corresponding to mode (2, 1) at $\Gamma = 1$. (*b*) Chaotic attractor at $\Gamma = 1.82$. (*c*) Sparse power spectrum of the limit cycle (*a*). (*d*) Full power spectrum of the chaotic attractor (*b*). Note the peaks at $N = \omega T/(2\pi) = 1$, corresponding to the forcing frequency. (*e*) Distance between points in phase space decreases exponentially for the limit cycle (*a*), indicating a Lyapunov exponent $\lambda \simeq -0.063$. All trajectories collapse onto the limit cycle. (*f*) For the chaotic attractor (*b*), the Lyapunov exponent $\lambda \simeq 0.4$. Initially neighbouring trajectories diverge exponentially, indicating sensitivity to initial conditions.

As Γ is increased, an increasing number of periodic solutions emerge. At $\Gamma = 1.2$, multi-periodicity arises, with modes (1,1), (2,1), (3,1) and (4,1) all coexisting. Further increasing Γ introduces a number of complex periodic modes, for example (3,3).

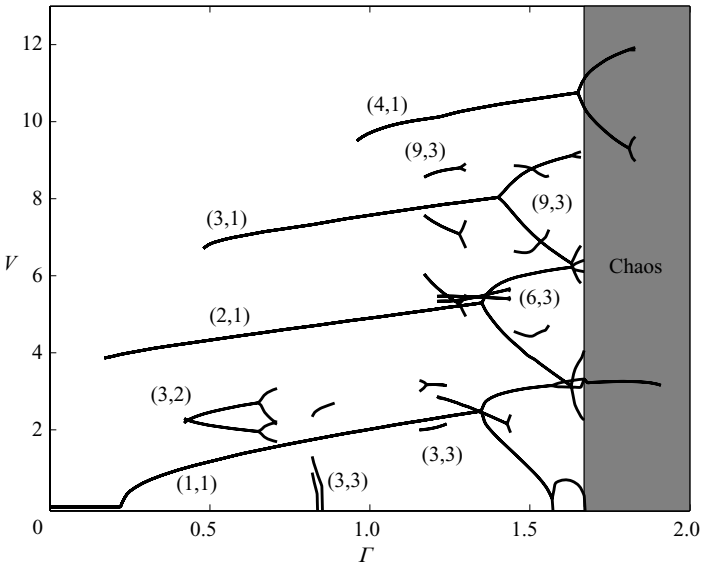

FIGURE 27. Bifurcation diagram for $\omega = 1.21$. Dimensionless impact speed V as a function of the dimensionless acceleration Γ, as deduced by integrating (4.14). No bouncing is observed below $\Gamma = 0.18$. Then, several discrete values of the impact velocity become possible, indicating multi-periodicity at moderate Γ. Finally, for $\Gamma > 1.76$ (shaded area), a few periodic states persist, but chaos prevails.

Finally, the principal modes $(m, 1)$ branch to $(2m, 2)$ states through period-doubling events; solutions then bounce between two branches on a vertical line in figure 27. The transition to chaos occurs via a number of such branching events, known as a period-doubling cascade. We note that modes $(2, 1)$ and $(3, 1)$ give rise to cascades that stop at roughly the same point $\Gamma \simeq 1.76$. The detailed cascade from $(2, 1)$ to $(64, 32)$ is represented in figure 28, and the accompanying power spectra clearly indicate period doubling. Within the predominantly chaotic regime ($\Gamma > 1.76$), some stable limit cycles still exist at least until $\Gamma = 1.9$. Further discussion of the bifurcation diagram is presented in Gilet & Bush (2008).

We note that in our experiments, both the appearance of complex modes and chaos occur for lower accelerations than in our model solutions. In particular, chaotic bouncing was observed at $\Gamma = 1.1$ in experiments (figure 14), instead of $\Gamma = 1.76$ in our simulations. This discrepancy is presumably due to the shortcomings of our simple model for the dissipation in the system; in particular, details of the droplet deformation are not modelled in (4.14).

Solutions of (4.14) can be displayed on a Poincaré section made at impact, i.e. $(y, \dot{y}, \theta) = (0, -V, \phi)$. Equations (4.14) are integrated numerically from one impact to the next, for various initial conditions (V, ϕ). A two-dimensional iterative map may thus be defined as

$$\left.\begin{aligned} V_{i+1} &= f(V_i, \phi_i), \\ \phi_{i+1} &= g(V_i, \phi_i). \end{aligned}\right\} \tag{4.15}$$

The net energy ΔE gained by the drop during the ith bounce is computed as the difference of kinetic energy between two successive impacts $\Delta E = (V_{i+1}^2 - V_i^2)/2$.

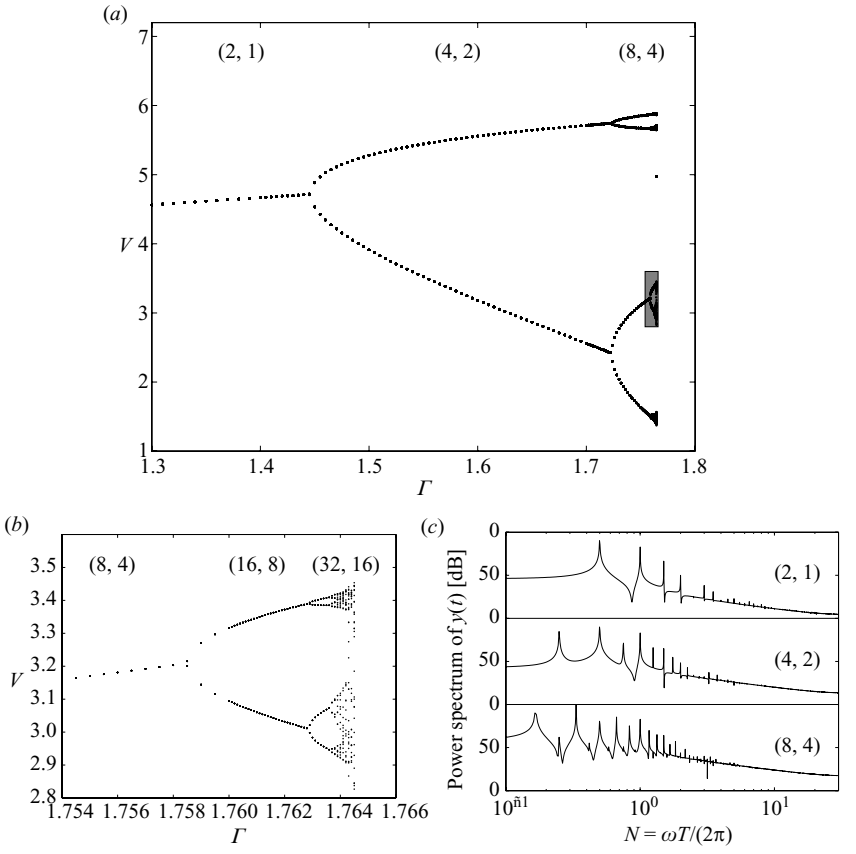

FIGURE 28. (*a*) Period-doubling cascade from mode (2, 1) to mode (64, 32) at $\omega = 1.1$. Dimensionless impact speed V as a function of the dimensionless acceleration Γ, as deduced by integrating (4.14). (*b*) Magnification of the shaded region in (*a*). (*c*) Power spectra of mode (2, 1) at $\Gamma = 1.33$, mode (4, 2) at $\Gamma = 1.5$ and mode (8, 4) at $\Gamma = 1.75$.

Results are presented in figure 29(*a–d*) for $\omega = 1.21$ and $\Gamma \in [0.6, 0.85, 1.3, 1.6]$. All the observed modes are represented in these iterative maps. Contours are iso-values of ΔE. For impact in the grey and white regions, the drop experiences a net energy gain and loss, respectively, during impact. On the intervening curve, the energy transferred to the drop precisely balances that dissipated, $\Delta E = 0$. Modes $(m, 1)$ are stationary states in this iterative map represented by single points that necessarily fall on this zero contour. We note that two or more equilibrium points may be found for each mode $(m, 1)$ on either side of the shaded area; however, numerical integration of (4.14) indicates that only points on the right-hand side of the shaded area are stable. We note that the shaded area is bounded above by a maximum-impact velocity, which explains, for example, why mode (4, 1) is impossible to observe at $\Gamma \leqslant 1.085$. Modes $(m, 1)$ observed experimentally at $\Gamma = 0.6$ are displayed in figure 29(*a*) for the sake of comparison. While the quantitative agreement is not exact, it is clear that our simple model captures the essential features of our experiments.

Complex modes $n > 1$ may also be rationalized with these iterative maps. Periodic modes are represented by closed circuits. The net energy extracted during all of the impacts along these circuits necessarily sums to zero. In modes $(m, 2)$, bouncing occurs

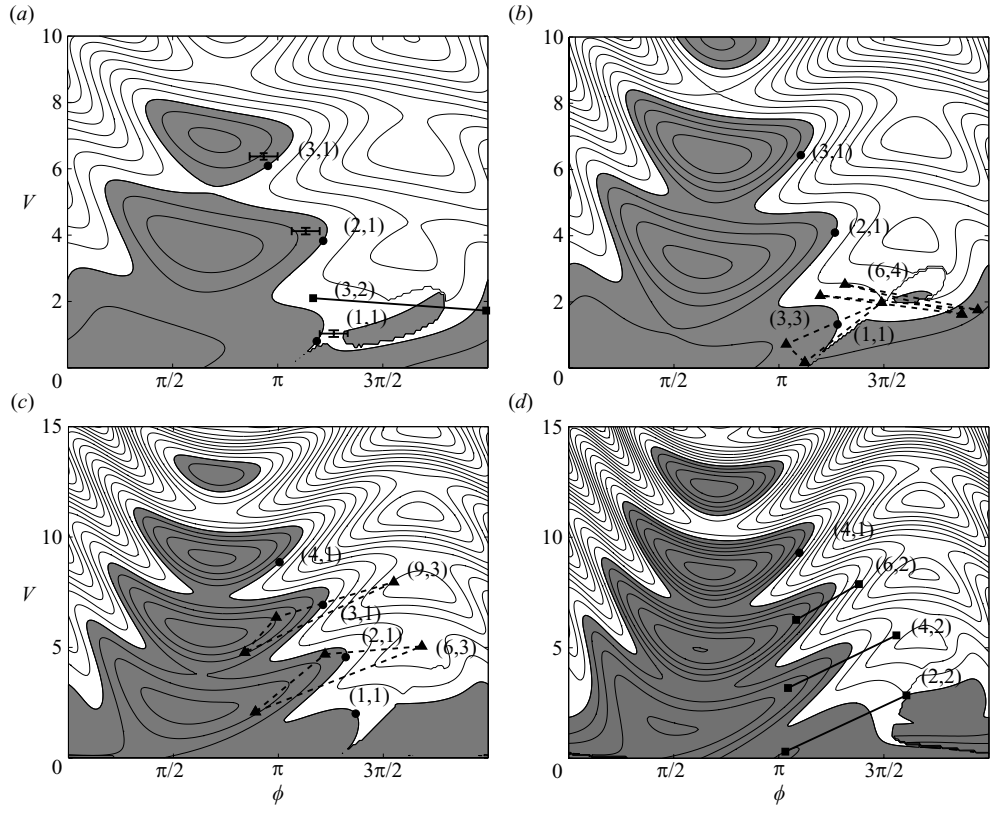

FIGURE 29. Net energy transferred to the drop during impact as a function of the impact speed V and phase ϕ. Poincaré sections at impact for several periodic states are superposed. The forcing frequency is $\omega = 1.21$, while the forcing acceleration is (*a*) $\Gamma = 0.6$, (*b*) $\Gamma = 0.8545$, (*c*) $\Gamma = 1.3$ and (*d*) $\Gamma = 1.6$, respectively. (●) Modes $(m, 1)$; (■) modes $(m, 2)$; (▲) modes (m, n) with $n > 2$. In the shaded area, computed numerically by integrating (4.14), the droplet gains more energy during impact than it loses to dissipation; in the white area, the opposite occurs. Energy contour curves are spaced by $\Delta E = 2$ in (*a,b*) and $\Delta E = 4$ in (*c,d*). Stationary periodic states $(m, 1)$ are presented along with closed orbits corresponding to complex periodic states. Crosses in (*a*) correspond to experimental data for modes $(m, 1)$ illustrated in figure 13.

alternately in- and outside the shaded area. For the (2,2) mode, evident in figure 29(*d*), the first bounce inside the shaded area transfers energy to the droplet, increasing the velocity at the second impact. The second bounce occurs outside the shaded area, so energy is lost. Energy, velocity and phase are thus decreased in order to restore the initial conditions to those of the first bounce. In mode (9, 3), two bounces increase the energy, the velocity and the phase until the droplet leaves the shaded region. The third bounce dissipates energy, thereby restoring the initial conditions of the first bounce. A Poincaré section of the chaotic attractor emerging at $(\omega, \Gamma) = (1.21, 1.82)$ is presented in figure 30. The structure of the chaotic attractor is represented in polar coordinates in figure 30(*b*).

In the limit of weak forcing and dissipation, $\Gamma \ll 1$ and $\Psi \ll 1$, (4.14) reduces to

$$\ddot{y_0} = -1 - y_0 H(-y_0), \tag{4.16}$$

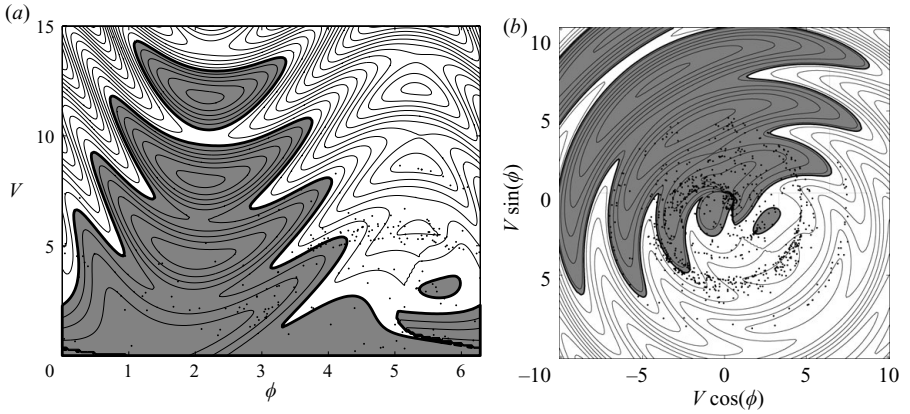

FIGURE 30. Poincaré section at impact of the chaotic attractor at $(\Gamma, \omega) = (1.82, 1.21)$. (*a*) Cartesian representation of the (V, ϕ) plane, with ΔE contours superposed (spaced by 5). The shaded area corresponds to a net gain of energy per bounce. (*b*) Polar representation of the (V, ϕ) plane, in which the detailed structure of the attractor is more clear.

which can be solved analytically subject to initial conditions $(y_0, \dot{y}_0) = (0, -V)$ at impact $\tau = 0$, yielding

$$y_0 = H(-y_0)[\cos\tau - 1 - V\sin\tau] + H(y_0)\left[V(\tau - \tau_1) - \frac{(\tau - \tau_1)^2}{2}\right], \tag{4.17}$$

where the dimensionless contact time $\tau_1 = t_c\sqrt{k/m}$ is given by

$$\tau_1 = 2\pi - 2\arctan V = 2\pi - 2\arctan\left[\frac{1}{\rho g R^2}\sqrt{\frac{3\sigma k We}{4\pi}}\right]. \tag{4.18}$$

We note that this prediction for the contact time is in excellent agreement with both our experimental observations (figure 11*a*) and numerical solution of (4.14).

The total period of a jump is given by the sum of the contact time and time in flight: $\tau_2 = \tau_1 + 2V$. For a periodic mode $(m, 1)$, the bouncing period must precisely match the forcing period, so that $\omega\tau_2 = 2\pi m$. We thus deduce a criterion for periodic bouncing modes $(m, 1)$

$$V_m - \arctan V_m = \pi\left(\frac{m}{\omega} - 1\right), \tag{4.19}$$

that prescribes the impact speed V_m required for each value of m to arise at a given forcing frequency ω. Note that $V - \arctan V$ increases monotonically with $V > 0$; therefore, $m > 1$ when $\omega > 1$. Consequently, this simple leading-order approach is not able to describe the mode (1,1), since it implicitly assumes that the forcing is weak. For mode (1,1), the amplitude of the forcing motion Γ/ω^2 has the same order of magnitude as the amplitude of the droplet motion $y(t)$.

For each value of the impact speed V and phase ϕ, the energy difference $\Delta E = E_{Supplied} - E_{Dissipated}$ may be computed for this reduced model via

$$\begin{aligned} E_{Dissipated} &= \Psi\int_0^{\tau_1} |\dot{y}_0|^3\,\mathrm{d}\tau \\ &= \frac{4\Psi}{3}\left[(V^2+1)^{3/2} + \frac{3}{2}V^2 + 1\right] \end{aligned} \tag{4.20}$$

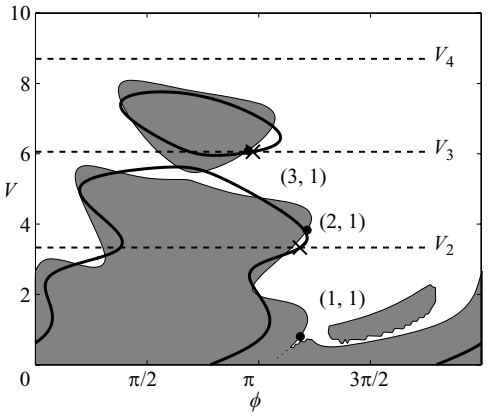

FIGURE 31. Net energy transferred to the drop during impact as a function of the impact velocity V and phase ϕ. The forcing parameters are $(\Gamma, \omega) = (0.6, 1.21)$. In the shaded area, computed numerically by integrating (4.14), the droplet gains energy during impact. The thick line is the leading-order approximation of the shaded area, corresponding to (4.20) and (4.21) deduced for a conservative, unforced system. Dashed lines correspond to velocities prescribed by the compatibility equation (4.19). Modes $(m, 1)$ predicted by numerical simulation are represented by dots and predictions based on the leading-order approach (4.20–4.21) are represented by crosses.

and

$$E_{Supplied} = \Gamma \int_0^{\tau_2} \dot{y}_0 \cos(\omega\tau + \phi)\, \mathrm{d}\tau$$
$$= \frac{2\Gamma}{\omega^2(\omega^2 - 1)} \left\{ \omega^2 \sin\left(\frac{\omega\tau_2}{2}\right) \left[\sin\left(\frac{\omega\tau_2}{2} + \phi\right) - \omega V \cos\left(\frac{\omega\tau_2}{2} + \phi\right) \right] \right.$$
$$\left. + \sin\left(\frac{\omega(\tau_1 + \tau_2)}{2} + \phi\right) [\omega V \cos(\omega V) - \sin(\omega V)] \right\}. \quad (4.21)$$

The resulting curve on which $\Delta E = E_{Supplied} - E_{Dissipated} = 0$ for $(\Gamma, \omega) = (0.6, 1.21)$ is displayed in figure 31. The analogous curve generated from the numerical solution of the full model system is included for the sake of comparison. While the results are qualitatively similar, the quantitative agreement is unsatisfactory. In particular, for low impact speeds, the solution of the unforced, conservative system yields a poor approximation for the neutral curve $\Delta E = 0$. Nevertheless, we can rationalize the absence of the (4,1) mode: according to the compatibility equation (4.19), $V_4 \geqslant 8.7$, which is beyond the shaded area for these low Γ values.

5. Discussion

We have presented a combined experimental and theoretical investigation of droplets bouncing on a soap film. We first considered droplet impact on a static film. Over the range of impact speeds considered, the film reacts rapidly to the external forces applied by the impacting drop. The film shape may thus be described as quasi-static, a spherical cap beneath the drop and a catenoid beyond it. This feature allows for the deduction of a simple force–displacement relation for the impacting drop that provides a good description of the drop trajectory. Moreover, it yields a criterion for droplet bouncing $We^* < 16$ that is consistent with our experimental

observations. Provided the droplet bounces, the film behaves like a linear spring with spring constant $k = (8\pi/7)\sigma$. Consequently, the contact time $\tau_c \sim \sqrt{m/k}$ is independent of impact speed. Finally, the droplet loses a certain percentage of its translational energy at each bounce, specifically $\Delta We = 0.087 We^{3/2}$: a fraction of the work done by the soap film is transferred into the vibrational energy of the droplet and subsequently lost through dissipation. These observations and deductions concerning the interaction of a droplet and a static film allowed us to make significant theoretical headway in characterizing the dynamics of droplets bouncing on a vibrating film.

The theoretical description of the bouncing dynamics is much simpler on a soap film than a liquid bath. In the configuration considered by Couder *et al.* (2005*a*), it is relatively difficult to characterize the precise shape of the fluid interface; moreover, describing the drop dynamics requires consideration of the motions within both the underlying fluid and the intervening air layer. Conversely, in our system, the intervening air layer serves only to communicate the curvature pressure from the film to the droplet; its dynamics may thus be neglected. When a droplet strikes a vertically vibrating reservoir, inertia determines the characteristic response time of the underlying fluid. On a vibrating soap film, the response of the interface to the droplet is effectively instantaneous; as a result, the contact time depends on neither the forcing frequency nor the impact speed.

On a vibrating film, the dissipative losses of a bouncing droplet may be balanced by the input of vibrational energy, so that periodic bouncing states can emerge. Simple and complex periodic bouncing states as well as multi-periodicity were observed. A simple theoretical model of the bouncing states was developed, and the essential physics of the process were captured. To describe the motion of the droplet's centre of mass, we deduced a single second-order nonlinear non-autonomous ordinary differential equation that reproduces all the bouncing states observed experimentally. Quantitative agreement was obtained between theory and experiment for the low-order periodic states, and qualitative agreement for the more complex periodic and chaotic states. More sophisticated modelling would incorporate the drop dynamics, treating explicitly the evolution of the droplet deformation.

The multiplicity of periodic bouncing solutions was rationalized by considering the energetics of the system. Since the contact time is independent of impact speed, the energy imparted to a droplet impacting a vibrating film is uniquely prescribed by the impact phase. Our model demonstrates that the different periodic modes arising at the same forcing parameters correspond to different impact phases. More complex modes were seen to correspond to closed orbits in the (V, ϕ) phase space (figure 29). Finally, we derived bifurcation diagrams to describe the dependence of the system behaviour on the forcing. As the applied acceleration Γ was increased progressively, the drop went through transitions from static, to simple periodic bouncing, to complex periodic bouncing states; ultimately, a number of period-doubling transitions lead to a chaos. The presence of chaos in our model system was confirmed by examining phase plots, power spectra and Lyapunov exponents.

The simplest fluid mechanical system that exhibits the features of low-dimensional chaos is the dripping faucet (Shaw 1984), whose dynamics have been investigated extensively (Ambravaneswaran *et al.* 2004; Coullet, Mahadevan & Riera 2005). The Howard–Malkus waterwheel (Strogatz 1994) is a fluid-driven mechanical device, the dynamics of which may be described in terms of the Lorenz equations (Sparrow 1982). The fluid trampoline, which we have shown to be analogous to a fluid mass on a fluid spring, may be numbered in this small group of simple fluid mechanical chaotic oscillators.

$a = t_c/\tau_c$	$Oh_{sf} \leqslant 0.015$	$Oh_{sf} = 0.13$
$Oh_d \leqslant 0.015$	1.86	1.38
$Oh_d = 0.13$	1.98	1.72
$b = \Delta We/We^{3/2}$		
$Oh_d \leqslant 0.015$	0.087	0.12
$Oh_d = 0.13$	0.082	0.097
$c = F_M/(\sigma R)We^{-1}$		
$Oh_d \leqslant 0.015$	1.11	0.57
$Oh_d = 0.13$	0.84	0.74

TABLE 3. Variation of (a) the contact time t_c, (b) the dissipated energy ΔWe and (c) the maximal force F_M with the viscosity of the droplet and the soap film as characterized by $Oh_d = \nu_d \rho_d / \sqrt{\sigma_d R}$ and $Oh_{sf} = \nu_{sf} \rho_{sf} / \sqrt{\sigma_{sf} R}$, respectively.

Finally, the manipulation of individual droplets is becoming progressively more important in microfluidics, and represents an attractive alternative to fluid displacement in microchannels (Stone, Stroock & Ajdari 2004; Squires & Quake 2005). Controlled droplet bouncing may be a promising way to manipulate fluids for microfluidic operations. We have seen that the bouncing of droplets on a soap film is markedly different from that on a bath, and much simpler to describe theoretically. It is hoped that our study will inform ongoing experimental and theoretical investigations of bouncing droplets.

T. Gilet thanks FRIA/FNRS and Belgian Government for financial support. We gratefully acknowledge Aslan Kasimov, Jeff Aristoff, Pedro Reis, Laurent Courbin, J-C Nave, Sunny Jung and Matt Hancock for fruitful discussions.

Appendix A. The role of viscosity

To assess the influence of viscosity on the system, the viscosity of both the droplet and soap film was varied. The resulting modifications to the contact time, energy dissipated and maximum force generated are reported in table 3. The constant of proportionality between the contact time t_c and the capillary time τ_c slightly increases with the droplet viscosity ν_d, and significantly decreases with increasing soap film viscosity ν_{sf}. The kinetic energy lost, ΔWe, increases with increasing soap film viscosity, and decreases with increasing droplet viscosity. The maximum force decreases with increasing drop and film viscosity.

We proceed by rationalizing the observed variation of dissipation with viscosity reported in table 3. When the drop viscosity increases, the drop becomes progressively more resistant to deformation (Clanet *et al.* 2004). Consequently, it becomes easier to deform the soap film than the drop, and the fraction of energy absorbed by droplet deformation Λ decreases. Since the dissipation coefficient (4.7) is proportional to $\Lambda^{1/2}$, it also decreases slightly. When the viscosity inside the film is increased, the contact time t_c/τ_c decreases, giving more importance to the phase where $F\dot{\eta} < 0$, thus increasing the energy transferred from translation to vibration. Dissipation is thus more efficient in the droplet, and the coefficient Λ increases.

Appendix B. Mode 2 droplet deformation

The theory of droplet oscillations was developed by Rayleigh (e.g. Landau & Lifchitz 1959). We present here some analytical results for the natural mode 2 deformation.

The potential velocity field is given in spherical coordinates by

$$\left.\begin{aligned} v_r &= C\cos(2\pi f t) r(3\cos^2\theta - 1), \\ v_\theta &= -3C\cos(2\pi f t) r\cos\theta\sin\theta. \end{aligned}\right\} \tag{B 1}$$

On the surface of the droplet, $r = R(\theta)$, and

$$\left.\begin{aligned} v_r &= \dot{R} = C\cos(2\pi f t) R(3\cos^2\theta - 1), \\ v_\theta &= R\dot{\theta} = -3C\cos(2\pi f t) r\cos\theta\sin\theta. \end{aligned}\right\} \tag{B 2}$$

The latter equation is directly integrated to give

$$\frac{\tan\theta}{\tan\theta_0} = \mathrm{e}^{-\frac{3C}{2\pi f}\sin(2\pi f t)}. \tag{B 3}$$

This result is substituted into (B 1) to find

$$\frac{R}{R_0} = \frac{\mathrm{e}^{\frac{C}{\pi f}\sin(2\pi f t)}}{\sqrt{\cos^2\theta + \mathrm{e}^{\frac{3C}{\pi f}\sin(2\pi f t)}\sin^2\theta}}. \tag{B 4}$$

This equation corresponds to a spheroid with vertical axis $c = R_0\mathrm{e}^{\frac{C}{\pi f}\sin(2\pi f t)}$ and equatorial radius $a = R_0\mathrm{e}^{-\frac{C}{2\pi f}\sin(2\pi f t)}$. We note that the volume of the spheroid is proportional to $ca^2 = R_0^3$ which does not depend on t: the volume of the droplet is conserved during its oscillation.

The surface area of the spheroid is given by

$$S = \begin{cases} 2\pi a^2 + \dfrac{2\pi a c^2}{\sqrt{c^2 - a^2}}\arcsin\left(\dfrac{\sqrt{c^2 - a^2}}{c}\right), & \text{if } c > a, \\ \dfrac{\pi}{\sqrt{a^2 - c^2}}\left[2a^2\sqrt{a^2 - c^2} + ac^2\ln\left(\dfrac{a + \sqrt{a^2 - c^2}}{a - \sqrt{a^2 - c^2}}\right)\right], & \text{if } c < a. \end{cases} \tag{B 5}$$

If we consider small deformations $c = R_0 + \eta$, $\eta \ll R_0$, the surface area becomes

$$S \simeq 4\pi R_0^2 + \frac{16\pi}{5}\frac{\eta^2}{2} + \vartheta(\eta^3). \tag{B 6}$$

The additional surface energy is thus given by

$$E_d \simeq \frac{8\pi}{5}\sigma\eta^2. \tag{B 7}$$

The kinetic energy of internal motions may be estimated from

$$K = \int_V \frac{\rho\left(v_r^2 + v_\theta^2\right)}{2}\,\mathrm{d}V \simeq \pi\rho\int_0^\pi \sin\theta\,\mathrm{d}\theta\int_0^{R_0}\left(v_r^2 + v_\theta^2\right)r^2\,\mathrm{d}r = \frac{4\pi}{5}\rho R_0^5 C^2\cos^2(2\pi f t). \tag{B 8}$$

Since $\eta = R_0 - R_0\mathrm{e}^{\frac{C}{\pi f t}\sin(2\pi f t)}$,

$$\dot{\eta}^2 = 4C^2R_0^2\cos^2(2\pi f t)\mathrm{e}^{\frac{2C}{\pi f}\sin(2\pi f t)} \simeq 4C^2R_0^2\cos^2(2\pi f t) \text{ if } C \ll 2\pi f, \tag{B 9}$$

so

$$K \simeq \frac{\pi\rho R_0^3}{5}\dot{\eta}^2 = \frac{3m}{10}\frac{\dot{\eta}^2}{2}. \tag{B 10}$$

Conservation of energy yields

$$\frac{\mathrm{d}}{\mathrm{d}t}(K + E_d) = 0 \rightarrow \frac{3m}{10}\ddot{\eta} + \frac{16\pi\sigma}{5}\eta = 0. \tag{B 11}$$

This harmonic oscillator has a frequency of $f = \sqrt{8\sigma/3\pi m}$, which is the exact expression obtained by Rayleigh from the dispersion relation of infinitesimal capillary waves.

Appendix C. Sources of dissipation

Some energy is inevitably dissipated in the air layer and the soap film. Both film and droplet are coated by a commercial surfactant whose precise surface properties are not easily quantified. The extent to which a surfactant-laden surface is rigidified depends on both the type and concentration of surfactant. In general, soap films lie between the 'rigid' and 'free' limits, in which the internal flows correspond, respectively, to Poiseuille and plug flows. The Poiseuille regime is more dissipative since velocity gradients arise across the thickness of the film. Conversely, in plug flow, transverse velocity gradients are negligible, and the dissipation results from velocity gradients in directions parallel to the film, which are necessarily much smaller. Therefore, for the sake of bounding the dissipation in the soap film, only the Poiseuille case is considered here.

Lubrication theory describes flows in a fluid domain that is very thin in one direction. The pressure gradients ∇p and the flow rate $\boldsymbol{Q}$ are effectively parallel to the film. Conservation of mass and momentum requires that

$$\frac{\partial h}{\partial t} + \nabla \cdot \boldsymbol{Q} = 0, \tag{C 1}$$

$$\boldsymbol{Q} + \frac{h^3}{12\mu}\nabla p = 0. \tag{C 2}$$

The energy dissipation ΔK in the whole film (surface S) during t_c is given by

$$\Delta K = -\int_0^{t_c}\int_S \boldsymbol{Q}\cdot\nabla p \,\mathrm{d}S\,\mathrm{d}t. \tag{C 3}$$

Equations (C 1) to (C 3) are scaled to yield

$$\left.\begin{aligned} \frac{h}{t_c} &\sim \frac{Q}{R} \\ Q &\sim \frac{h\Delta p}{12\mu R} \end{aligned}\right\} \Rightarrow \begin{cases} Q^2 \sim \dfrac{12\mu R^4}{t_c^3\Delta p} \\ h^2 \sim \dfrac{12\mu R^2}{t_c\Delta p}, \end{cases} \tag{C 4}$$

while the dissipation scales as

$$\Delta K \sim t_c(2\pi R^2)\frac{\Delta p}{R}Q \sim 4\pi\sqrt{\frac{3\mu R^6\Delta p}{1.86\tau_c}}, \tag{C 5}$$

where Δp is the anomalous air pressure in the air layer beneath the drop's centre. We thus deduce

$$\Delta We \sim \frac{3\Delta K}{2\pi R^2\sigma} \sim 6\sqrt{\frac{3\mu R^2\Delta p}{1.86\tau_c\sigma^2}}. \tag{C 6}$$

The overpressure Δp should scale as $F_M/(\pi R^2) \sim 0.35\sigma/RWe$, which gives a scaling for the dissipated energy,

$$\Delta We \sim 3Oh^{1/2}We^{1/2}. \tag{C 7}$$

Assuming that the constant of proportionality is relevant, the range of energy loss due to dissipation in a soap film with $Oh = 0.015$ is $\Delta We \in [0.37, 1.5]$, while the observed range of dissipation is $\Delta We \in [0.2, 5]$. So, for $We \lesssim 1$, we expect the resulting dissipation in the soap film to be relevant for the case of rigid films. This additional source of dissipation might explain the fact that the observed dissipation is systematically higher than the scaling law (2.4) for $We \sim 1$. Nevertheless, the scaling $\Delta We \sim We^{1/2}$ is not observed experimentally for $We \gtrsim 1$.

The Ohnesorge Oh_a based on the air viscosity is approximately 100 times less than Oh; therefore, the dissipation in air is negligible. The typical thickness reached by the air layer during impact is inferred from (C 4)

$$\left(\frac{h}{R}\right)^2 \sim \frac{12\mu_a}{t_c\Delta p} \sim 9\frac{Oh_a}{We}, \tag{C 8}$$

which yields $h \in [7, 28]$ μm for We in the range [1, 16]. Note that if the film is free, the air layer drains more easily and thins more rapidly.

REFERENCES

Ambravaneswaran, B., Subramani, H. J., Phillips, S. D. & Basaran, O. A. 2004 Dripping–jetting transitions in a dripping faucet. *Phys. Rev. Lett.* **93**, 034501.

Biance, A. L., Chevy, F., Clanet, C., Lagubeau, G. & Quéré, D. 2006 On the elasticity of an inertial liquid shock. *J. Fluid Mech.* **554**, 47.

Blanchette, F. & Bigioni, T. 2006 Partial coalescence of drops at liquid interfaces. *Nature Physics* **2**, 254.

Boudaoud, A., Couder, Y. & Ben Amar, M. 1999 Self-adaptation in vibrating soap films. *Phys. Rev. Lett.* **82** (19), 3847.

Charles, G. E. & Mason, S. G. 1960*a* The coalescence of liquid drops with flat liquid/liquid interfaces. *J. Colloid Sci.* **15**, 236.

Charles, G. E. & Mason, S. G. 1960*b* The mechanism of partial coalescence of liquid drops at liquid/liquid interfaces. *J. Colloid Sci.* **15**, 105.

Chen, X., Mandre, S. & Feng, J. J. 2006 Partial coalescence between a drop and a liquid–liquid interface. *Phys. Fluids* **18**, 051705.

Clanet, C., Béguin, C., Richard, D. & Quéré, D. 2004 Maximal deformation of an impacting drop. *J. Fluid Mech.* **517**, 199.

Couder, Y. & Fort, E. 2006 Single-particle diffraction and interference at a macroscopic scale. *Phys. Rev. Lett.* **97**, 154101.

Couder, Y., Fort, E., Gautier, C. H. & Boudaoud, A. 2005*a* From bouncing to floating: noncoalescence of drops on a fluid bath. *Phys. Rev. Lett.* **94**, 177801.

Couder, Y., Protière, S., Fort, E. & Boudaoud, A. 2005*b* Walking and orbiting bouncing droplets. *Nature* **437**, 208.

Coullet, P., Mahadevan, L. & Riera, C. S. 2005 Hydrodynamical models for the chaotic dripping faucet. *J. Fluid Mech.* **526**, 1.

Courbin, L., Marchand, A., Vaziri, A., Ajdari, A. & Stone, H. 2006 Impact dynamics for elastic membranes. *Phys. Rev. Lett.* **97**, 244301.

Courbin, L. & Stone, H. 2006 Impact, puncturing and the self-healing of soap films. *Phys. Fluids* **18**, 091105.

Dell'Aversana, P., Banavar, J. R. & Koplik, J. 1996 Suppression of coalescence by shear and temperature gradients. *Phys. Fluids* **8**, 15.

Dorbolo, S., Terwagne, D., Vandewalle, N. & Gilet, T. 2008 Resonant and rolling droplets. *New J. Phys.* **10**, 113021.

Gilet, T. & Bush, J. W. M. Chaotic bouncing of a droplet on a soap film. *Phys. Rev. Lett.* **102**, 014501.

Gilet, T., Mulleners, K., Lecomte, J.-P., Vandewalle, N. & Dorbolo, S. 2007*a* Critical parameters for the partial coalescence of a droplet. *Phys. Review* E **75**, 036303.

Gilet, T., Terwagne, D., Vandewalle, N. & Dorbolo, S. 2008 Dynamics of a bouncing droplet onto a vertically vibrated interface. *Phys. Rev. Lett.* **100**, 167802.

Gilet, T., Vandewalle, N. & Dorbolo, S. 2007*b* Controlling the partial coalescence of a droplet on a vertically vibrated bath. *Phys. Rev.* E **76**, 035302.

Graff, K. F. 1975 *Wave Motion in Elastic Solids*. Oxford University Press.

Honey, E. M. & Kavehpour, H. P. 2006 Astonishing life of a coalescing drop on a free surface. *Phys. Rev.* E **73**, 027301.

Jayaratne, O. W. & Mason, B. J. 1964 The coalescence and bouncing of water drops at an air–water interface. *Proc. R. Soc. London, Ser.* A **280**, 545.

Kowalik, Z. J., Franaszek, M. & Pieranski, P. 1988 Self-reanimating chaos in the bouncing-ball system. *Phys. Rev.* A **37** (10).

Landau, L. & Lifchitz, E. 1959 Fluid mechanics. In *Course on Theoretical Physics*, vol. 6. Addison Wesley.

Legendre, D., Daniel, C. & Guiraud, P. 2005 Experimental study of a drop bouncing on a wall in a liquid. *Phys. Fluids* **17**, 097105.

LeGoff, A., Courbin, L., Stone, H. A. & Quéré, D. 2008 Energy absorption in a bamboo foam. *Europhys. Lett.* **84**, 36001.

LeGrand-Piteira, N., Brunet, P., Lebon, L. & Limat, L. 2006 Propagative wave pattern on a falling liquid curtain. *Phys. Rev.* E **74**, 026305.

Lieber, S., Hendershott, M., Pattanaporkratana, A. & Maclennan, J. 2007 Self-organization of bouncing oil drops: two-dimensional lattices and spinning clusters. *Phys. Rev.* E **75**, 056308.

Lorenz, E. N. 1963 Deterministic nonperiodic flow. *J. Atmos. Sci.* **20**, 130.

Mahajan, L. 1930 The effect of the surrounding medium on the life of liquid drops floating on the same liquid surface. *Phil. Mag* **10**, 383.

McLaughlin, J. B. 1981 Period-doubling bifurcations and chaotic motion for a parametrically forced pendulum. *J. Stat. Physics* **24** (2), 375.

Mehta, A. & Luck, J. M. 1990 Novel temporal behavior of a nonlinear dynamical system: the completely inelastic bouncing ball. *Phys. Rev. Lett.* **65** (4), 393.

Neitzel, G. P. & Dell'Aversana, P. 2002 Noncoalescence and nonwetting behavior of liquids. *Annu. Rev. Fluid Mech.* **34**, 267.

Okumura, K., Chevy, F., Richard, D., Quéré, D. & Clanet, C. 2003 Water spring: a model for bouncing drops. *Europhys. Lett.* **62** (2), 237–243.

Pan, K. L. & Law, C. K. 2007 Dynamics of droplet–film collision. *J. Fluid Mech.* **587**, 1.

Protière, S., Boudaoud, A. & Couder, Y. 2006 Particle–wave association on a fluid interface. *J. Fluid Mech.* **554**, 85.

Protière, S., Couder, Y., Fort, E. & Boudaoud, A. 2005 The self-organisation of surface waves sources. *J. Phys. Cond. Mat.* **17**, S3529.

Richard, D., Clanet, C. & Quéré, D. 2002 Contact time of a bouncing drop. *Nature* **417**, 811.

Richard, D. & Quéré, D. 2000 Bouncing water drops. *Europhys. Lett.* **50** (6), 769.

Shaw, R. 1984 *The Dripping Faucet as a Model Chaotic System*. Aerial Press.

Sparrow, C. 1982 *The Lorenz Equations: Bifurcations, Chaos and Strange Attractors*. Springer.

Squires, T. & Quake, S. R. 2005 Microfluidics: fluid physics at the nanoliter scale. *Rev. Mod. Phys.* **77**, 977.

Stone, H. A., Stroock, A. D. & Ajdari, A. 2004 Engineering flows in small devices: microfluidics towards a lab-on-a-chip. *Annu. Rev. Fluid Mech.* **36**, 381.

Strogatz, S. 1994 *Nonlinear Dynamics and Chaos, with Applications to Physics, Biology, Chemistry and Engineering*. Perseus Books.

Taylor, G. I. & Howarth, L. 1959 The dynamics of thin sheets of fluid. I. Water bells. *Proc. Roy. Soc.* A **253**, 289.

Taylor, G. I. & Michael, D. H. 1973 On making holes in a sheet of fluid. *J. Fluid Mech.* **58**, 625.

Terwagne, D., Vandewalle, N. & Dorbolo, S. 2007 Lifetime of a bouncing droplet. *Phys. Rev.* E **76**, 056311.

Thoroddsen, S. T. & Takehara, K. 2000 The coalescence cascade of a drop. *Phys. Fluids* **12** (6), 1265.